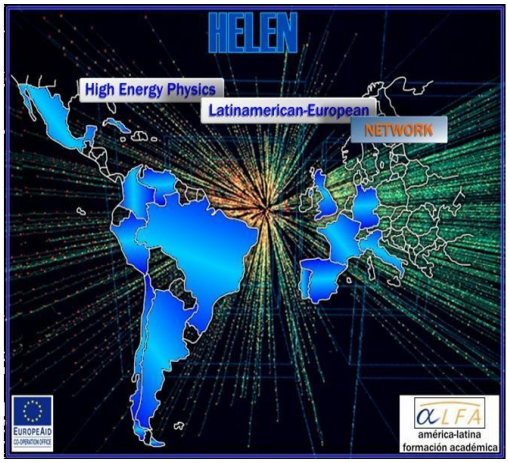

Contribution to the commissioning of the ATLAS calorimeter electronics calibration

Br. Antonio L. Cárdenas G.

Tutor: Dr. Lydia Iconomidou-Fayard

LAL-Laboratoire de l'Accélérateur Linéaire
CNRS/IN2P3-Universite Paris XI, Orsay, France.
Centro de Física Fundamental, Departamento de Física,
Facultad de Ciencias, Universidad de Los Andes,
Mérida, Venezuela

Mayo 2008
Mérida - Venezuela

I would like to thank:

The HELEN project (High Energy physics Latinamerican-European Network) for giving me this opportunity to be involved in the high energy physics domain, a field that, experimentally, is not yet found in Venezuela (but it begins!!).

The people involved in it that makes it possible for us to do this, specially Jose Ocariz, whose ENORMOUS patience and good will was able to handle even the most terrible bureaucratic barrier ('Enredos BURROcraticos' sería más correcto!). The discutions we had helped me a lot in the understanding of what I was doing.

Lydia.. WOW! I just couldn't have a better tutor, and I mean it. Even in the very difficult times (for both..) you were there to help me out, with enough patience and will to teach me most of the things I know now. Hereusement tu n'est pas devenue chèvre, même avec toutes mes bêtises (surtout être très très très en retard comme d'habitude!). Je suis vraiment reconnaissant de tout ce que tu as fait pour moi, merci! Je n'oublirais non plus ta merveilleuse cuisine (oh la la! Louis a TROP de chance!), dont il me faudra encore quelques recettes...

Les autres membres du groupe ATLAS du LAL, qui m'ont fait sentir comme un d'eux: Daniel, Louis, Abdenour, Marumi, Laurent, RD, Dirk, Luc, David, Patrick ... Je suis content d'avoir pu faire des amis aussi: Fanny, Francesco, Henso, Pauline, Dimitrios, Iro, Matt[3], Emmanuel, Nikola, Ilija... I learned a lot and had great times!!

A Luis y Alejandra, que han sido más que profesores excepcionales sino también guías que me han traido hasta donde estoy. Sin sus consejos, ayuda y enseñanzas no hubiese logrado hacer esta tesis, son realmente unos maestros!

Al resto de profesores que me han ayudado directa o indirectamente aportandome sus enseñanzas y consejos a lo largo de mi carrera, en especial a Nelson, Hector[2], Adel, Marcos y Noemi.

To my friends on both sides of the ocean for your great support and the great times! I'm lucky, really lucky to be able to say that the list would be too long for their name to be put here. But you know who you are! (including old friends, fisicos, biologos et parisiens!).

A mi familia, especialmente mi mama, mi papa y mi hermana, cuyo apoyo incondicional es lo mejor que tengo en mi vida y que me han dado lo necesario para ser quien soy y seguir adelante... Gracias!

Contents

1 Introduction

The Standard Model of Particles has been able, so far, to describe accurately the physics domain called 'Particle Physics'. This domain includes all the experimental research for the understanding the most elementary of particles, the quarks (components of protons and neutrons) and the leptons (as the electrons and neutrinos), and their mutual interactions. But the SM theory does not seem to describe everything, and some parts of it have not yet been well understood or observed at physics experients. One of the missing pieces is a particle called the 'Higgs' boson, which could explain why particles have a mass and why they are so different. To be able to find and 'see' this particle we must look at very high energies, and so to prove new physics models and discover new particles. This search for so called 'very rare events' needs very fast and precise detectors.

And so, the will to put in evidence particles as the top quark (seen at the end of 1993 at Fermilab) or the Higgs boson motivated the construction of a new particles accelerator, the LHC, and of the ATLAS detector found at CERN. The measurement of high energetic particles at accelerators with many events per collition (High Luminosity), needs a reconstruction able to select fast enough the events of interest and to write them in a reliable data base.

To identify the electrons and photons in ATLAS, the Electromagnetic Calorimeter was concieved, which participates in the reconstruction of collition events and energy measurement. The timing calibration of this apparatus is necessary to avoid false events reconstructions and to be able to sample correctly the energy values of the incident particles. The study of the noise given by the electronic chain also allows a better data reconstruction and the identification of related problems.

The second chapter describes the Standard Model and the LHC, giving a glimpse on the different components of the ATLAS detector, while the third chapter gives further details on the electromagnetic calorimeter and the signal paths and calibration.

The fourth and fifth chapters correspond to the work done at LAL-Orsay on the Electronic Calorimeter Calibration, thanks to the HELEN fellowship. The fourth describes some timing analysis done to understand the different contributions on the arrival time of the calibration signal and it's shape, and the fifth chapter shows the study of the shape and stability of the Noise Autocorrelation Function and it's effectivity for bad channels identification on the electromagnetic calorimeter.

2 The Standard Model, The LHC and ATLAS

2.1 The Standard Model

Particle physics is modelized by a theory called the Standard Model of Particles, introduced in 1967 by Glashow, Weinberg and Salam. This theory describes the elementary components of matter and their interaction, and most of it's consistency has been proved in different experiments. Nature has been explained so far with 4 fundamental forces: gravity, weak force, electromagnetism and the strong nuclear force; each one carried out by a particle, a gauge boson, wich are the graviton, the $W^{\pm}$ and Z^0, the photon and the gluons respectively. Electromagnetism and the weak force form the electroweak force, and the Standard Model describes their unification. [1]

2.2 Elementary Particles

The elementary components of matter are called elementary particles, and they are classified in two categories: the fermions and the bosons. The fermions are the constituants of matter, having half integer spin and are ruled by the Fermi-Dirac statistics and the Pauli's exclusion principle, wich means that two fermions can not be on the same quantum state. The bosons are the 'carriers' of the interactions between particles, having an integer spin and are ruled by the Bose-Einstein statistics, in wich 2 or more bosons can be at the same quantum state.

2.2.1 Fermions

Fermions are divided in two categories: the leptons and the quarks, each one divided in three families or generations. The first family consists of the particles that build our world. The difference between these three families is essentially the mass of the particles in them, wich increases from the first to the third family, and this cannot be explained by the Standard Model.

Table 1: Fermions Properties

Leptons			Quarks		
Flavor	Mass GeV/C^2	Electric charge	Flavor	Approx. Mass GeV/C^2	Electric charge
ν_e (electron neutrino)	$< 7 \times 10^9$	0	u_{up}	0.005	2/3
e (electron)	0.000511	-1	d_{down}	0.01	-1/3
ν_μ (muon neutrino)	< 0.0003	0	c_{charm}	1.5	2/3
μ (muon)	0.106	-1	$s_{strange}$	0.2	-1/3
ν_τ (tau neutrino)	< 0.03	0	t_{top}	170	2/3
τ (tau)	1.7771	-1	b_{bottom}	4.7	-1/3

Leptons have an integer charge and do not experience the strong interaction, being able to exist

as free particles. Quarks have a fractionary charge, they experience all four fundamental forces but have never been seen as free particles, they form structures of integer charge called hadrons. These structures can be made of a quark and an antiquark, then they're called mesons, or of three quarks, then called baryons. Dirac equation allow the existence of particules with negative energy, called antiparticles, of positive energy but opposite electrical charge. Each particle has then an associated antiparticle, the positron e^+ for the electron by example.

2.2.2 Bosons

Bosons can be either elementary, like the photon, or composite, as mesons. As particles with integer spin, mesons are considered like strongly interacting bosons. All force carrier particles are elementary bosons, two particles interact due at the exchange of a boson carrier of the interaction. There are four interactions, one for each fundamental force:

- Strong Interaction
  Acts on quarks and it is responsible for their confinement in the hadrons. There are eight gluons carriers of this interaction, and their behaviour can be explained in quantum chromo dynamics.

- Electromagnetic Interaction
  Happens between two electrical charged particles and it is carried out by the photons. It creates an attractive force between opposite charged particles, and repulsive if they have identical charge.

- Weak Interaction
  Is responsible for β decays at low energies and it is carried by three bosons: Z^0, W^+ and W^-, that were discovered at CERN in the 80's.

- Gravitational Interaction
  Is carried out by the graviton and it is responsable for the gravitational response. It is not included in the Standard Model for it has never been seen.

Table 2: Force Carriers

Force	Particle(s)	Mass GeV/c^2	Electric charge
Electromagnetic	Photon (γ)	0	0
Weak	W^-	80.22	-1
	W^+	80.22	+1
	Z^0	91.187	0
Strong	Gluon (g)	0	0

2.2.3 The Higgs Boson

The Standard Model has given evidence so far of being a correct and consistent theory of particle physics. Indeed, no experiment has been found to be inconsistent with it. However a key element

is missing, the Higgs boson has not been detected yet, which is believed to be responsible for the spontaneus breakdown of gauge symmetry, and wich gives mass to the gauge bosons and fermions. Its discovery would be a triumphant confirmation of the Standard Model in its entirety, for its existence has now been predicted for more than three decades. Why has it not be seen by any experiment so far? The answer lies on its mass, and to the preferentil coupling it has to heavy particles. In order to have a chance to see the Higgs we need higher energy collisions, a new generation of particle physics experiments.[1]

2.2.4 Constraints on the Higgs boson mass

The Standard Model cannot predict the Higgs boson mass, but there are theoretical and experimental limits on its value. Theoretical limits are based in arguments of finite cross section and consistency of the theory, with a heaviest Higgs of 700 GeV. The experimental limits come from the direct search of the Higgs boson at LEP (Large Electron-Positron Collider, CERN), where it was not found for a mass smaller than 114.4 GeV, with a certainty of 95 percent. Combination of all the precise electro-weak meausurements made at LEP, Tevatron and SLC, constraint m_h to be between 115 and 251 GeV.

2.3 Unanswered Questions of the Standard Model

Even if the Standard Model has not yet been proved wrong by the experiments so far, it is known that it is not the final theory for particle physics, for it does not provide, in its actual form, several important answers. Some of the topics that remain unanswered are:

- The hierarchy of the fermion masses: why are there 4 orders of magnitude between the lightest and the heaviest quark? Why neutrinos have a negiglable mass compared to the others fermions? The Higgs mechanism could provide hints to these questions.

- The high number of free parameters (18) found in the theory, as masses and coupling constants. It might represent a hint as to why we have started thinking that the Standard Model is just part of a larger model, that will unify electroweak interaction with the strong and gravitational one.

- The origin of the electro-weak symetry violation. At the begining, the universe contained matter and anti-matter in equal amounts, why did the anti-matter disappear? Hints for this could be found on the CP (Charge conjugation and Parity) violation search.

2.4 The Large Hadron Collider

The Large Hadron Collider (or LHC) is the largest particle accelerator ever conceived, and it is currently under tuning at CERN (European Organization for Nuclear Research) near Geneva,

Switzerland[2]. It is placed in the 27 km long tunnel wich formely housed LEP, but in contrast to LEP, LHC will collide not electrons and positrons, but protons and protons. The beam energy of LHC will be around 7 TeV, corresponding to a centre-of-mass energy of 14 TeV. It's main goals are to find the Higgs boson and look at the region of mass around TeV to find proof of eventual new physics.

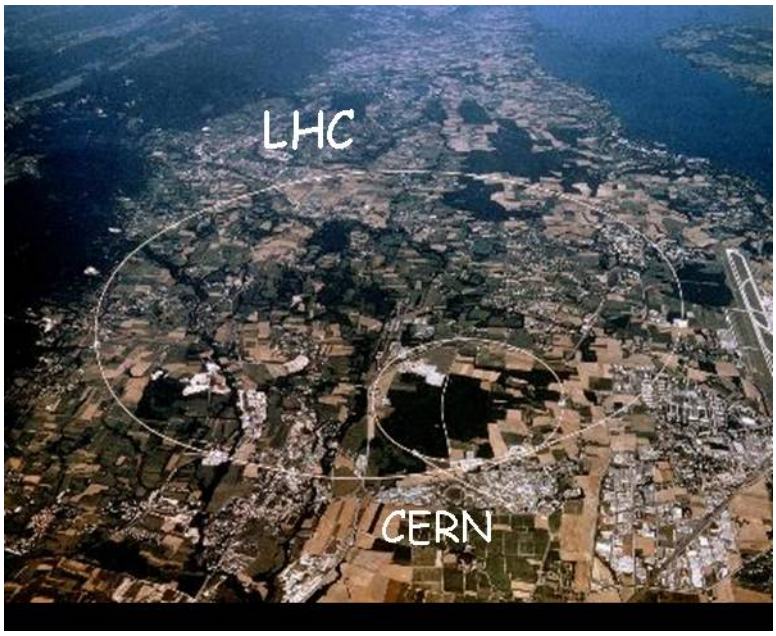

Figure 1: The LHC at CERN

CERN's network of previous accelerators allows production and pre-acceleration of particles before their injection into the LHC. Protons are created using hydrogen and are initially accelerated by a Linear Accelerator up to 50 MeV, then by 3 successive circular accelerators, the Booster up to 1 GeV, the PS (Proton Sycrhoton) up to 26 GeV and finally the SPS (Super Proton Synchroton) up to 450 GeV. The protons are later injected into the main LHC ring and accelerated up to 7 TeV. Protons will be assembled in bunches. Inside the LHC there will be 2808 bunches per ring (2, each per opposite direction) spaced at a distance of 7.48 m, corresponding to a time interval of 24.95 ns. Each of these bunches will contain 1.05×10^{11} protons. This time interval between bunches give us a measure of the collision rate expected at the LHC. The number of events N_{evt} produced per second is given by:

$$N_{evt} = L\sigma_{evt} \tag{1}$$

where σ_{evt} is the effective section of the studied process and L is the luminosity of the accelerator. Luminosity relies only on the parameters of the beam and can be written as:

$$L = \frac{N_b^2 n_b f_{rev} \nu_r}{4\Pi\epsilon_n \beta^*} F \tag{2}$$

where N_b is the number of particles per bunch, n_b the number of bunches per beam, f_{rev} the revolution frequency, ν_r the relativistic factor of particles, ϵ_n the normalized transverse emmitance

of the beam, β^* the β function at the collition point, and F a geometrical factor to reduce the luminosity due to the beam crossing angle at the interaction point =0.9. On the first data taking period, that lasts three years, the luminosity will be low, L_0=10^{33}cm^{-2}s^{-1}, and the next years it will be raised to L_0=10^{34}cm^{-2}s^{-1}. At expected luminosity, in each crossing a mean of 24 inelastic interactions may happen. Most of these events are of no interest, for the energy transfered between crossing partons is low and the particles created at final state have a weak transverse impulse. These are called 'minimum bias' events and they overlap the interesting events of weak cross section. The minimum bias events are the source of pile-up, putting some difficulty at the design of the detectors. The pile-up effect is bigger when the response time of the detector is higher than the bunch crossing time, so it's necessary to have a very fast and reliable lecture system. An appropiate treatement of the signal can reduce the pile-up effect, as it will be seen for the electromagnetic calorimeter.

A series of superconductive magnets were developed to curve the particle beams. These are composed of a magnetic cylinder head and a cryogenic infrastructure, wich keeps the head at a temperature of 1.9 K by using super fluid liquid helium. The head produces a magnetic field of 8.4 T within the two beam pipes. To obtain the desired collisions the beams wil cross at 4 points, that represents the location of the detectors that will measure the product of such collisions: ATLAS, CMS, LHCb and ALICE. The first two are general purpose detectors, while LHCb was created for the study of b-quark physics and ALICE for the study of quark-gluon plasma physics by colliding heavy ions, mainly lead nuclei.

2.5 The ATLAS detector

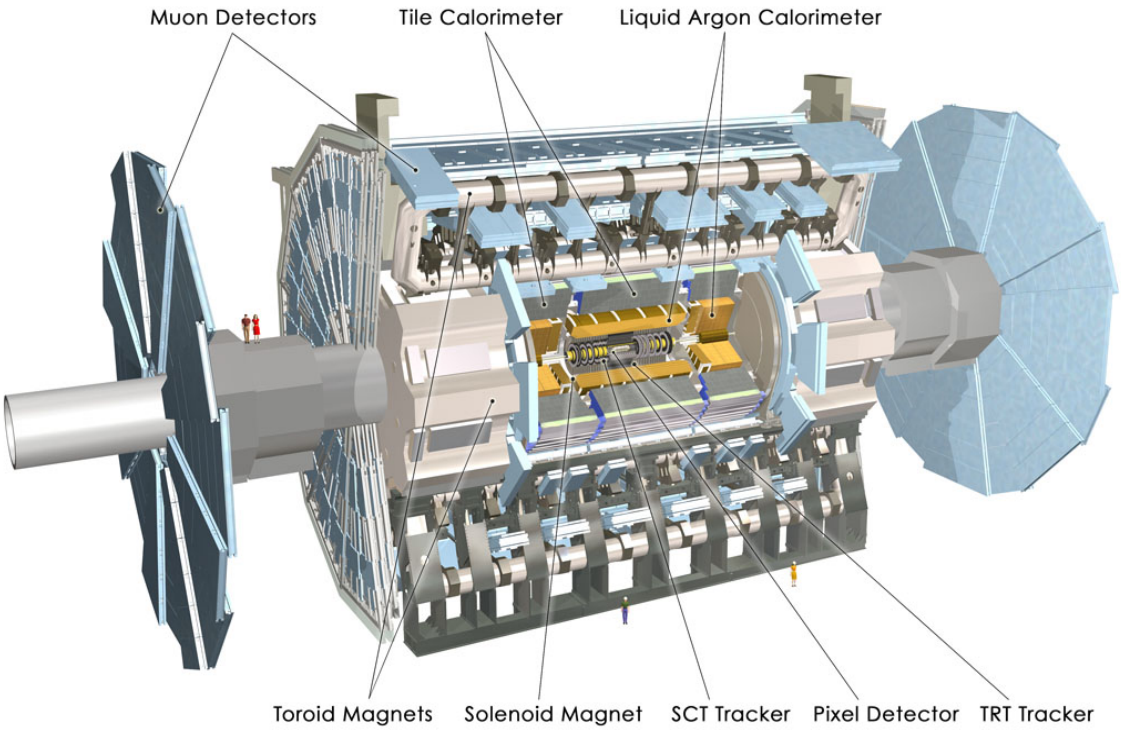

Figure 2: The ATLAS detector and its components

The ATLAS detector is one of the two general purpose detectors at LHC. Its main goals are the Higgs boson search and looking at the new physics that may come out of collisions. It's designed as a classical 4Π detector with cylindrical symmetry and different components build up as layers, making 50 meters long and 25 meters of diameter, weighting aproximately 7000 tonnes. The central part, called barrel, is completed at it's ends by two caps that close the solid angle around the beams interaction point. From the interaction point, the different components are: the Inner Tracker which measures the momentum of each charged particle, the Calorimeters that measure the energies carried by the particles, the Muon spectrometer which identifies and measures muons, and the Magnet system that bends charged particles for the momentum measurement.The Higgs boson at ATLAS could be found looking at its desintegration channels, specially it's desintegration in 2 photons ($H \rightarrow \gamma\gamma$) or 4 leptons ($H \rightarrow ZZ^* \rightarrow 4l$).

2.5.1 The Coordinate System

The z-axis (Oz) is defined by the beam direction, and the transverse plane to the beam defines the x-y plane (xOy). The azimuthal angle ϕ is measured on the transverse plane xOy around the beam, and the polar angle θ is measured on the longitudinal plane, and it's the angle between the particle's trajectory and Oz. However, in the hadronic colliders, instead of using the normal polar angle θ,

an angular quantity called pseudorapidity η is employed, related by the following equation:

$$\eta = -\ln\left(\tan\left(\frac{\theta}{2}\right)\right) \tag{3}$$

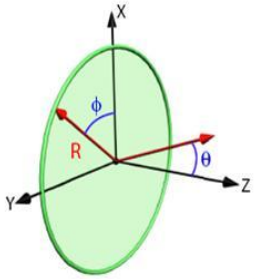

Figure 3: The coordinate system

It's a good variable to approximate the rapidity if the mass and momentum of the particle are unknown. The rapidity is defined as:

$$y = \frac{1}{2}\ln\left(\frac{E + p_L}{E - p_L}\right) \tag{4}$$

Where p_L is the longitudinal momentum and E is the energy of the incident particle. The rapidity is only valid when the mass of the particle is negligeable for it's impultion.

The particles flux at collisions is constant per rapidity unit. That's why the sub-detectors are segmented by η so there's a constant occupation rate on the different lecture channels.

2.5.2 The Inner Detector

The tracking system or Inner detector is 7 meters long and extends to a radius of 1.2 meters. Its purpose is to track charged particles by detecting their interaction with materials at discrete points, revealing crucial information about the particle's type, charge and momentum. The mechanism consists of a magnetic field that surrounds the inner detector and causes charged particles to curve; the direction of the curve gives the particle's charge while the radius of curvature gives its momentum, using the expression p=qBr, where p is the magnitude of the momentum, q is the electric charge, B the magnitude of the magnetic field and r the radius of curvature found.

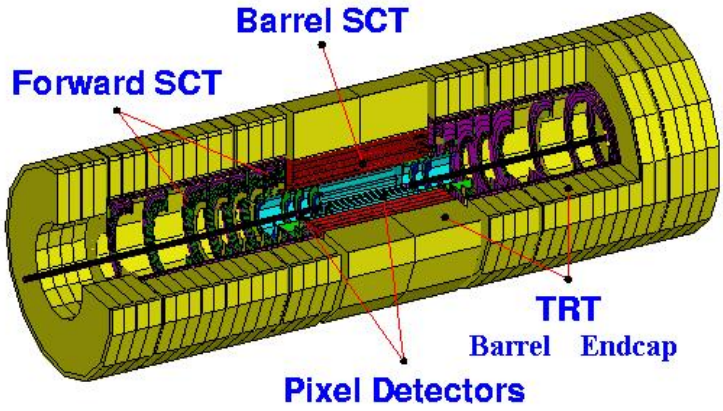

Figure 4: The inner detector and its components

The inner detector has three main components:

- The pixel detector: It's the innermost part of the detector, having 3 cylindrical layers in the barrel and 3 disks on each end-cap, for 1744 modules in total. A considerably small pixel size is intended for extremely precise tracking very close to the interaction point. Due to its proximity to the interaction point, the pixel detector is subject to a great deal of radiation so all the components had to be radiation hardened in order to operate properly. Each time a charged particle traverses one of the layers, a signal is produced, giving a precise measurement of the particle's position and thereby determine whether the particle originated at the collision, or a few millimeters from it as a result from a decay product of another particle. This is better known as vertex.

- Semi-Conductor Tracker (SCT): It's the middle part of the detector, similar in concept and function to the preceding part of it. It allows a large covered area with reduced granularity. It's designed to contribute to the measurement of momentum, impact parameter and vertex position. The STC is composed of four double layers of silicon strips and can provide eight precision measurements per track in the intermediate radial range, covering $\eta < 2.5$.

- Transition Radiation Tracker (TRT): The outermost part of the detector, is a combined straw tube tracker and transition radiation detector. It consists of several tens of thousand radial straws. Each straw is filled with a gas that is ionized whenever charged particles pass through. The ions are drawn to the inner wall of the straw, while the electrons go to a wire kept at high potential creating a current. This creates a pattern of signals within several straws that allow to determine the path of the particle. The straws also contain materials with different indexes of refraction, and causes charged particles to leave much stronger signals in each straw by producing transition radiation, which gives it a standalone electron identification capability. The TRT provides 36 two-dimensional measurements points in average, with 0.170 mm resolution for charged particles tracks with $|\eta|$ <2.0 and $p_T > 0.5$.

2.5.3 ATLAS Calorimeters

Lying outside the solenoidal magnet that surrounds the inner detector we find the two calorimeters in ATLAS: The electromagnetic and the Hadronic calorimeters. Their main purpose is to measure the energy from particles by stopping them, taking place with the development of a shower, which is a cascade of secondary less-energetic particles that produce even more particles with lesser energy and so forth, due to their interaction with dense matter, until the particles produced have an energy small enough to be absorbed by the interacting material. There are two types of showers studied in the calorimeters, the electromagnetic and the hadronic showers.

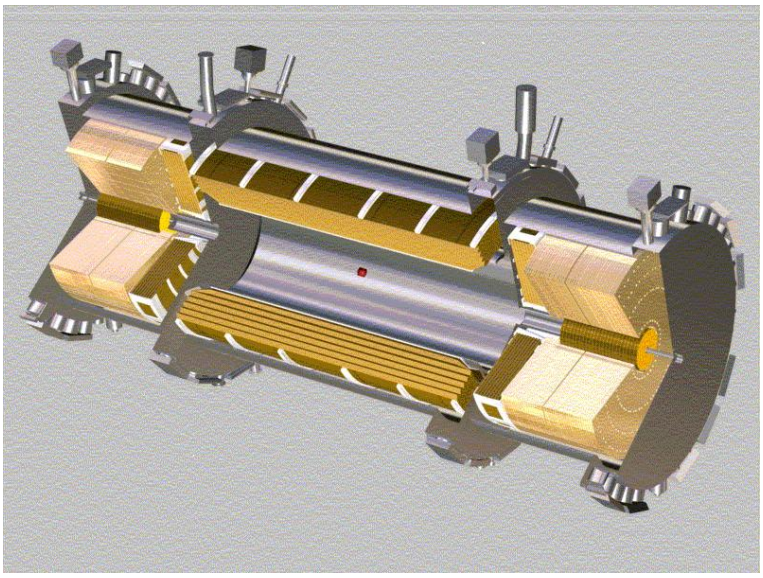

Figure 5: Electromagnetic Calorimeter

- Electromagnetic Calorimeter: it's the first you found when looking outside from the interaction point, just outside the solenoidal magnet that surrounds the inner detector. It's a sampling calorimeter with accordeon-shaped lead electrodes. Pre-samplers consisting of one layer of LAr are found in front of the calorimeter to correct for the energy lost in front of the calorimeter, due mainly to the cryostat walls and the barrel solenoid. Only particles that interact electromagnetically deposit most of their energy in this calorimeter, mainly photons and electrons (or positrons). The electromagnetic calorimeter is able to localize to a certain extent the particles that pass through it. The principles and components of the LAr electromagnetic calorimeter will be explained with further details on chapter 2.

- Hadronic calorimeter: Just after the electromagnetic calorimeter, it meaures the energy from showers produced by hadrons. It's composed of two main parts, the tile calorimeter and the liquid argon end cap hadronic calorimeter. The tile calorimeter is a large sampling calorimeter that makes use of steel as absorber material and scintillanting plates. The range covered is $\eta < 1.7$. The scintillating tiles are placed on perpendicular planes to the colliding beams and staggered in depth. High energy hadrons interact in the plates and transform the incident energy into a hadronic shower. These showers causes the scintillating tiles to emit light in a

proportional amount to the incident energy. The liquid argon end cap hadronic calorimeter uses similar principles as the electromagnetic one but using copper plates, instead of lead plates, more appropiate to the hadronic showers. The argon gaps are also twice as large. Total radiation emanating from the collision point is less intense at small values of η, and more intense at greater values. As scintillating tiles are damaged by excessive radiation, hadronic calorimetry is provided by this device for regions of $\eta > 1.7$.

2.5.4 Muon Spectometer

Basically an enormous chamber tracker, it's tremendous size is required to accurately measure the momentum of muons wich traverse the other parts of the detector without being stopped. Muons are a key element in a number of physical processes and the total energy of particles could not be measured accurately if they were ignored. Muons curve for their momentum to be measured, with a different magnetic field, lower spatial precision and a quite larger volume.

2.5.5 Magnet system

The magnet system has two principal components, the Central Solenoid and the Toroid Magnet.

- Central Solenoid: It's 5.3 m in length and has an inner diameter of 2.4 m. It's designed to provide a 2 T field in the central tracking volume, and could reach a peak value of 2.6 T. The conductor is made of a flat superconducting cable located at the center of an aluminium stabilizer with a rectangular cross-section. The solenoid shares the cryostat with the LAr Calorimeter to reduce some material buid-up.

- Toroid Magnet: It consists of eight barrel coils housed in separate cryostats and two end-cap cryostats housing eight coils each. In order to provide radial overlap and to optimize the bending power in the interface regions of both coil systems, the en-cap coil systems are rotated by 22.5° with the barrel toroid. The lack of uniformity on the magnetic field produced agrees with the much less precise measurements needed to measure the momentum accurately in the muon system.

2.5.6 Trigger System

LHC beams have a bunch cross frequency of 40 MHz and at high luminosity there'll be a mean of 24 events. Much of these events are of no interest (minimum bias events), and having a limited storage rate it's vital for the experiment to be able to filter most of them, and preserve only interesting events. The event rate must be lowered by a 10^7 factor, simply because it's the event rate at wich data can be written to permanent storage. This is the main purpose of the Trigger system with the Data Aquisition System (DAQ), composed of three selection levels:

- Level 1 (LVL1): the filtering is made using partial data from the sub-detectors, having a less precise granularity. Only events where leptons, photons and reconstructed jets contain high

P_T, a very large missing transverse energy or total scalar transverse energy are kept. The biggest difficulty is to treat incoming signals of an event having a lot more are acquired during that treatment time. The events rate goes from 40 MHz to 75 KHz. The selected events are then read by the 'front' electronics, located on top of the detectors, and go through the ROD (readout drivers) then the ROB (readout buffers) where data is kept waiting for the next filtering step. This data are transmitted to the next level as Region of Interest (RoI), including position (η and ϕ) and transverse energy of cadidate particles, and the transverse energy sum (total and missing energy).

- Level 2 (LVL2): using RoI data it filters events using complete information from subdetectors (but only for these regions of interest). Seleccion criteria are a lot more restrictive to obtain a data rate of 1 kHz.

- Level 3 (Event Filter, or EF): this final trigger level makes use of algorithms and reconstruction methods taking calibration and alignement data of detectors and the magnetic field board. This is a more subtle selection, achieving an event rate of 100 Hz.

Events are then definitely stored for a later offline analysis.[3]-[4].

3 The Electromagetic Calorimeter and Calibration Signal

The electromagnetic calorimeter plays a main part on the ATLAS experiment, having to measure with great precision the energy of electrons and photons and provide data to the first level trigger. It also has to measure the energy of jets and the missing transverse energy of particles. To achieve the great performances needed, good technics must be employed in a complex environment: high level of radiation and the need of a fast detector response.

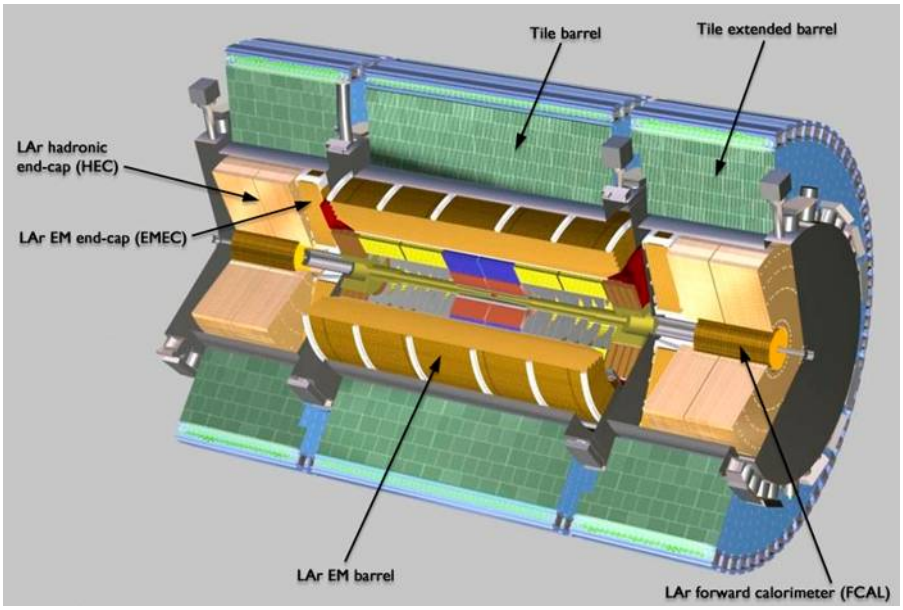

Figure 6: ATLAS Calorimeters

The idea of the electromagnetic calorimeter with accordeon shape of the ATLAS experience and its following design had as main purpose the best analysis of physics traces, highly linked to the discovery of the Higgs boson and supersymmetry. For this, the calorimeter must accomplish some objectives [5]:

- A great pseudorapidity ($|\eta|$) coverage to maximize the signal efficiency and a minimum of dead zones (zones without data taking) to allow a good measurement of the missing transverse energy.

- A fine granularity to increase the statisitical meaning of rare processes, as $H \rightarrow \gamma\gamma$ and $H \rightarrow 4l$.

- An excellent way to identify electrons and photons and a strong jets rejection, which needs a very thin granularity of at least $\Delta\eta \times \Delta\phi = 0.025 \times 0.025$ on the pseudorapidity region of $|\eta| < 2.5$, and a separation in several compartments, one with a thinner granularity in η to put appart γ/π^0.

- A very good energy resolution between 10 and 300 GeV to achieve a mass resolution of $\approx 1\%$ for the $H \rightarrow \gamma\gamma$ and $H \rightarrow 4l$ processes.

- To be able to identify the crossings at level 1 trigger, a time resolution of a few ns for a signal of about 1 GeV is needed. For higher energies a resolution of about 100 ps is necessary to be able to detect events with 'late' photons, and then measure their lifetime.

Looking at simulation and beam tests results, the ATLAS electromagnetic calorimeter satisfies all these requirements. Most of them have been put together for the discovery of the Higgs boson in some particular channels. In the energy region between 114.4 GeV (minimum imposed by the LEP experiences) and $2m_z \cong 180GeV$, the most favorable desintegration channel, $H \rightarrow b\bar{b}$ (90%), is very difficult to see due to noise contribution, but the $H \rightarrow \gamma\gamma$ and $H \rightarrow 4l$ chanels show evident sign, but with a smaller probability of appearance, which imposes most of the previous requirements.

3.1 Liquid Argon (LAr) Calorimetry

A sampling liquid argon calorimeter is an alternation of absorbing layers (in this case Pb) dense enough to degrade the energy of an incident particle, with gaps filled with liquid argon where an electrode is submerged to collect the ionisation signal applying an electric field. When a high energy particle goes through the absorbing material it starts an electromagnetic shower.

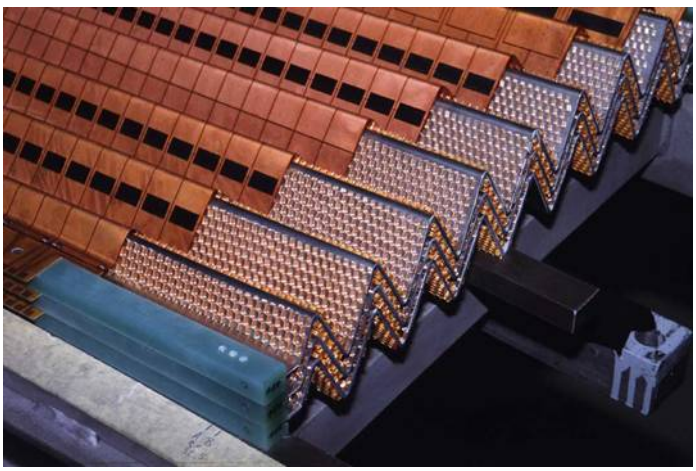

Figure 7: The accordeon shaped EM calorimeter

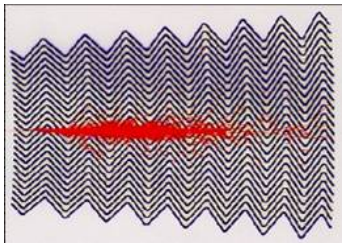

Figure 8: Electromagnetic Shower

The energy of the incident particle decreases in the interactions, creating electrons and positrons of smaller energy. At the end of the shower, the final number of particles created is proportional to the incident's particle energy. Over 100 MeV, the two main processes wich contribute to the development of the shower are the Breemsstrahlung ($e^{\pm} \rightarrow e^{\pm} + \gamma$) and the Pair Production ($\gamma \rightarrow e^{+} + e^{-}$). The shower is stopped when the energy of the particles is below an critical energy ($E_c \approx 10Mev$ for LAr), where ionisation processes take over the radiation ones, inhibiting the shower. In the liquid argon, particles coming from the electromagnetic shower lose a fraction of their energy via ionization: $e^{-} + A_r \rightarrow e^{-} + A_r^{+}/e^{-}$. The number of A_r^{+}/e^{-} pairs produced is proportional to the energy deposited in the liquid argon. This energy fraction is aproximately 15%. 2000 volts are applied between an electrode, that works as a cathod, and the lead absorber, used as ground. This voltage creates a current in the liquid argon with the ionisated electrons, which move faster than the A_r^{+} ions. This current inducts a signal on the lecture electrode which is led out the detector, and its intensity is proportional to the energy of the shower particles in the liquid argon. To calibrate the detector it is necessary to understand the relationship between the collected current and the energy of the incidental particle.[7]

3.2 Calorimeter description

The ATLAS electromagnetic calorimeter is composed of two central parts ($z > 0$ and $z < 0$) called half-barrels and two cap parts to close the calorimeter endings. The barrel parts of the calorimeter cover the pseudorapidity region of $|\eta| < 1.475$ and are contained in a cryostat 6.8 m large, internal radius of 1.15 m and external one of 2.25 m, while the en-caps cover the region $1.375 < \eta < 3.2$, placed at $z = \pm 4.3m$.

3.2.1 The barrel

Each half barrel is arbitrarily divided in 16 identical modules made independently, for technical reasons, and assembled to make the barrel. The absorbers and electrodes follow an accordion geometry, giving the fast response, noise reduction and a total ϕ hermeticity necessary for the transverse missing energy measurement. Each electrode is 275 μ thick, and it's constituted of three copper layers separated by two kapton layers. The two external layers are putted at 2000 volts, and the internal one is where the current inducted by the electrons in the LAr is collected. The distance between the lead absorber and the electrode is 2.1 mm, and constant for the whole barrel. The lecture electrodes are projectively segmented on η to be able to point out to the beam cross zone. They are also grouped in cells on ϕ, and radially segmented into three sections: front,

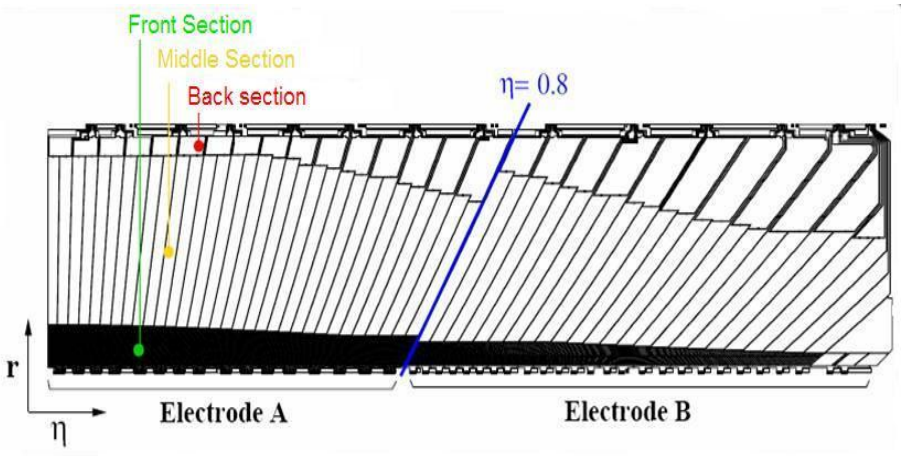

Figure 9: Eletrode Scheme showing its segmentation .

middle and back.

The front section is very thinly segmented on η, and composed of 451 detection cells commonly called strips. These cells are labeled in numbers, from 0 on the first and 450 on the last one. The fine granularity $\Delta\eta = 0.003 radian$ on η allows a precise measurement of the impact zone of particles to separate the spatially close electromagnetic jets (rejection of $\pi_0 \rightarrow \gamma\gamma$). On ϕ the granularity is less accurate, each cells covers a $\Delta\phi = 0.1 rad$. It's 2.464 cm in depth aproximately.

The middle section has 57 cells on η, labeled from 0 to 56. It's granularity $\Delta\eta \times \Delta\phi = 0.025 \times 0.025$ allows the measurement of the polar incident angle θ of particles, with the information given by the front section. It's 10,08 cm in depth aproximately, which allows it to contain most of the electromagnetic shower of a 50 GeV photon.

The back section has 27 cells on η, labeled from 0 to 26, with a granularity $\Delta\eta \times \Delta\phi = 0.05 \times 0.025$. It's main purpose is to estimate the energy loss on the back of the detector due to late electromagnetic showers. It's minimum depth is 1.12 cm, having to reduce the depth of the first 10 middle cells to provide it.

A pre-sampler is placed just before the lecture services of the electromagnetic calorimeter, to estimate the energy loss due to death material in the calorimeter. Its granularity is $\Delta\eta \times \Delta\phi = 0.025 \times 0.1$. As the pseudorapidity increases, the lead lenght crossed by the incident particles increases as well. In order to keep a constant radiation lenght for the middle section cells, the thickness of the lead absorbers change at $|\eta| = 0.8$, going from 1.5 mm for smaller values to 1.1 mm to bigger ones. This also makes the cells change their shape, and be able to separate an A part $|\eta| < 0.8$ and a B part $|\eta| > 0.8$ of the electrode.

3.2.2 The end cap

The end-cap section of the calorimeter uses the same liquid argon technology and the same accordion geometry than the barrel section, and each of the two end-caps is put on a 3.17 m long cryostat with 2.25 m of external radius. They consist of two concentric wheels, the external covering $1.4 < \eta < 2.5$ and the internal one the region $2.5 < \eta < 3.2$. It has a pre-sampler, front, middle and back section with different granularities as for the barrel.[5]

3.3 Energy resolution of the Electromagnetic Calorimeter

The energy resolution of the electromagnetic calorimeter can be parametrized as:

$$\frac{\sigma\left(E\right)}{E} = \frac{a}{\sqrt{E}} \oplus \frac{b}{E} \oplus c \tag{5}$$

where the energy E is in GeV. The first term (a) takes into account the stochastic fluctuations of the electromagnetic shower development in the liquid argon. It's value it's about 10%, depending on the homogenity of the sensitive material and the sampling fraction of the detector.

The second term (b) is due to electronics noise and it's value is between 300 MeV and 500 Mev, depending on the luminosity.

The constant term (c) takes into account the detector non-uniformities or instabilities and the error on the calibration, and this limits the high energy performance. A great effort must be made to contain its effect. It must be lower than 0.7%. It's contributions can be seen on the next board.[7]

Origin	Contribution
Local Term	0.35%
Mechanics	0.3%
Calibration	0.25%
Non-homogenities in temperatures	0.2%
Total	0.6%
Limit	0.7%

Table 3: Contributions to the c term for the energy resolution

3.4 Electromagnetic Calorimeter Calibration

To obtain a costant term (c) inferior to 0.7% in the energy resolution of the electromagnetic calorimeter channels a precise calibration system is used to equalize and follow the energy response of all cells.The same system allows to test the connectivity and the stability of the electronic components. The detailed physics signal shape in a cell can be derived through an electrical model, knowing the calibration pulse-shape. Then, a particle energy deposited in a cell can be reconstructed using Optimal Filtering Coefficients (OFC).

In the following we will quikly describe the physics signal and the way the calibration signal is obtained to be quite similar.

3.4.1 Description of the LAr Signal

Triangular Signal The electric field applied between a reading electrode and an absorber collects the charges produced in the Argon ionisation. This inducted current has a triangular shape in function of time:

$$I(t) = \frac{Q_0}{t_d}\left(1 - \frac{t}{t_d}\right) \tag{6}$$

where t_d is the mean drift time of the eletrons in the Argon, of about 400 ns, and Q_0 is the total charge deposited in the Argon. The maximum of the signal is proportional to the quantity of charges created in the liquid argon and so to the energy deposited by the shower. It follows a copper path on the reading electrodes and gets to the front and back sections where summing boards add the signals comming from the different electrodes with different ϕ granularity. These signals are then transmitted, using mother boards, outside the cryostat to the Front End Boards. The mother boards are put just in front of the summing boards to support them and are also in charge of the calibration signal distribution.

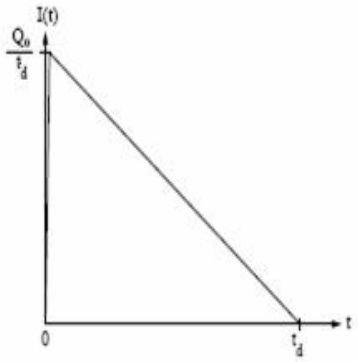

Figure 10: Typical shape of the induced current of a particle on an electrode.

Preamplification and shaping On the FEB, the triangular signal is amplified using preamplifiers to obtain a signal with a level higher than the noise level of the whole electronic chain that follows. These preamplifiers put a condition on the total electronic noise of the readout chain. Then the signal goes to the shapers, which are actually bi-polar filters of the $CR - RC^2$ type, and give the signal the characteristic bi-polar shape. This minimises the contribution of minimum bias events as it has a long signal decrease. Indeed, the integral value being null after the shaping, the contribution of the pile-up signals is null too. The two integrations allow the filtering of the high frequencies and then reduce the electronic noise. The shaping time is then a mix between reducing the electronic and the pile up noise, having found a value of $T_s = 15ns$ at high luminosity.

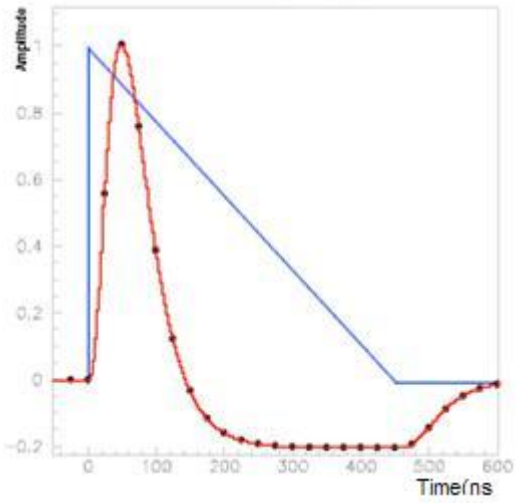

Figure 11: Physics signal before (blue) and after (red) shaping. The black dots are samples.

The shaping also produces three signals, each for a differen dynamic range of energy covered called 'gains' due to the encoding of the signal received. The three signals are amplified with three different gains (low, middle and high) on the order of 1/9.3/93.

Sampling After the shaping process, the signals are sampled every 25 ns, with an adjustable phase, and the third sample (out of only 5 that are kept) must be found at the maximum of the signal with $\pm 2ns$. All these samples are kept in an analogical pipeline waiting for a desition of the level 1 trigger. An analogical circuit chooses the optimal amplification gain using the third sample value. When the trigger desition is made, the samples are transmitted to an analog/digital converter (ADC), and then via optical link to the Read Out Driver (ROD) for the energy reconstruction. The unit used to measure the signals after the ADC output is commonly called 'ADC counts'.[6]

3.4.2 Description of the Calibration Path

The calibration signal follows a similar but still different path than the physics one. It also has some differences on it's shape due mainly to supplementary inductances used and the calibration cables. The signals are generated in the calibration boards for each channel to check the conectivity and response for each one of them, and be able to obtain some values used on the RODs for the energy reconstruction.

From a calibration pulse obtained in a cell, one can predict the expected physics pulse using a electrical model taking into account of the small differences beetwen calibration and physics currents and tracks.

Calibration Board The calibration board has as final purpose to establish the ADC↔current correspondance. It injects a signal at the beginning of the readout chain, as if it was the ionisation

signal, when this one is not present. A Digital/Analog converter (DAC) produces a voltage, transformed in a D.C. current that goes through an inductance (RL circuit); its discharge simulates the triangular signal through a decreasing exponential.

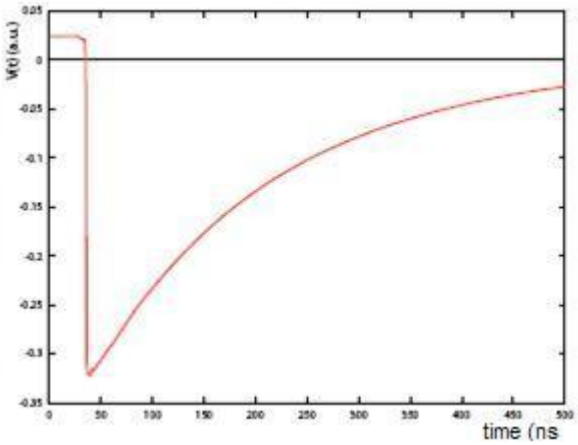

Figure 12: Signal generated on the calibration board, before shaping.

The signal is injected into the electrodes using an injection resistance R_{inj}, and goes through all the readout chain until its convertion in ADC. An special procedure is used to determine the ADC↔DAC correspondance, called the 'ramp' procedure, which consists in taking a few different DACs and to measure it's ADC response, that can be parametrized using a polinomial. This response is essentially linear and it's slope can give the wanted correspondance.[6] Knowing the correspondance ADC↔DAC (ramp), DAC↔voltage and voltage↔current (fonction of R_{inj}), it's easy to obtain the main correspondance ADC↔energy with the last factor current↔energy, obtained after test and simulation measurements.

It's important to notice the difference between the signal send by the calibration board and the signal coming from the ionization, one is exponential and the other is triangular.

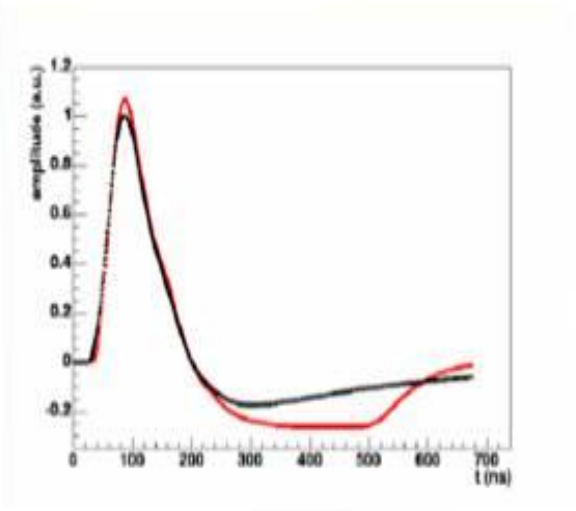

Figure 13: Difference between calibration (black) and physics signal (red) after shaping.

Electronic noise and pedestal When there's no energy deposited in the cells, the electronic chain gives a signal for each readout channel. That's what's called pedestal, and it allows to measure the energy fluctuations. Indeed, for every channel the signal varies from an event to the next following a gaussian distribution, due to the noise found in the electronic chain of the signal. This noise depends on the gain of the shapers and it's simply called 'electronic noise'. It's meausured on pedestal runs on a given gain. This can be written out as:

$$\text{Pedestal} = < E_{ADC} >$$
$$\text{Electronic Noise} = \sqrt{< E_{ADC}^2 > - < E_{ADC} >^2} = \sigma$$

Where E_{ADC} is the signal in ADC counts without energy deposit.

Cross talk and Pile up Noise There are two other effects affecting the signal: The cross talk and the Pile up Noise. The cross-talk is the signal of a cell induced by the neighbors cells, being of the same compartment or not. The pile up noise is simply the contribution of signals coming from minimum bias events, of lower energy than the interesting signal to which they overlap. The total noise is the quadratic sum of all the noises.

Calibration Procedures Different kind of measurements are made with the calibration system[7]:

- Pedestal measurements: when no signal is sent, the response on the readout chain is measured. This allows the evaluation of the electronic noise of the system, and the calculation of the autocorrelation matrix between runs.
- Ramp procedure: measures the cell response, particularly the maximum of the signal (in ADC counts) for a serie of signals with increasing DAC on the three gains. This allows a correlation between the given DAC and its value at the end of the readout chain. The

adjustment by a second degree polinomial allows to take into account some non-linear effects on the DAC-ADC correspondance.

- Delays Procedure: After shaping the signal is sampled every 25 ns. A delay circuit found on the calibration board allows to delay the signal sending by 1 ns step. Sending several signals this way, for the same DAC value but increasing delays, we can sample the whole signal and be able to reconstruct its shape.

3.4.3 At the Read Out Driver (ROD)

The Read Out Driver (ROD) boards, after receiving the ADC samples and the information from the calibration boards, digitally perform the Optimal Filtering described further on. Then they send the signal as an energy, time, and data quality triplet to the Read Out Buffer (ROB) modules, which are the entrance to the Data Adquisition system. If the event is selected by the trigger system then the data will be stored on disk.

Optimal Filtering Here we will describe the OFC method to obtain the energy value using 5 sampings along a signal.

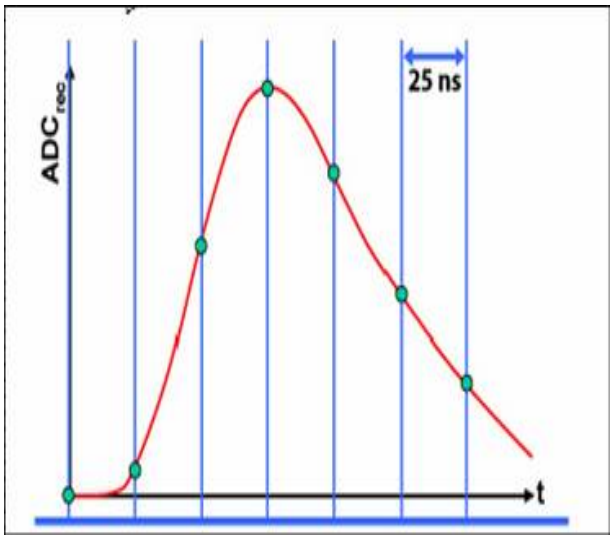

Figure 14: A signal sampled every 25 ns. Only the 5 samples around the maximum (3rd sample) are taken on the OFC method for the energy reconstruction.

The ADC samples are recombined by balancing them with calculated coefficients using the Optimal Filtering method, this to minimize the effect of the electronic and pile up noise, and to secure the codition that a time delay of the signal doesn't change the results. The observed signal is given in function of time by[8]:

$$S(t) = Ag(t+\tau) + n(t) \approx Ag(t) + A\tau g'(t) + n(t) \tag{7}$$

where A is the amplitude of the signal and g defines its shape, g' is the time derivate of g, and τ is the time shift, supposed small enough for the approximation to be valid, and $n(t)$ is the noise contribution. The samples at time t_k, which have the same time difference, corresponding to the different bunch crossings, can be written as:

$$S_k \cong Ag_k + A\tau g'_k + n_k \tag{8}$$

The optimal filtering method consists in minimise the variance of both values:

$$U = \sum_k a_k S_k \quad where \quad < U >= A \tag{9}$$

$$V = \sum_k b_k S_k \quad where \quad < V >= A_\tau \tag{10}$$

The a_k and b_k coefficients are called Optimal Filtering Coefficients (OFC). Knowing that the noise has a mean null value ($< n_k >= 0$), these equations lead to the following conditions:

$$\sum_k a_k g_k = 1 \qquad \sum_k a_k g'_k = 0 \tag{11}$$

$$\sum_k b_k g_k = 0 \qquad \sum_k b_k g'_k = 1$$

With these conditions the variances of U and V are:

$$Var(U) = \sum_{j,k} a_j a_k AC_{jk} \tag{12}$$

$$Var(V) = \sum_{j,k} b_j b_k AC_{jk} \tag{13}$$

with $AC_{jk} =< n_j n_k >$ corresponding to the Noise Autocorrelation matrix. Using the Lagrange multipliers method, a vectorial expression of the OFC can be written as:

$$a = \frac{(g'.Rg')Rg - (g.Rg')Rg'}{(g.Rg)(g'.Rg') - (g.Rg')^2} \tag{14}$$

$$b = \frac{(g.Rg)Rg' - (g.Rg')Rg}{(g.Rg)(g'.Rg') - (g.Rg')^2} \tag{15}$$

where the matrix R is the inverse of the autocorrelation matrix AC. With these OFC samples, the energy and the time difference (the time of the event) are reconstructed. In ATLAS only 5 samples will be used, centered in the maximum of the bi-polar curve.

We saw that computing OFCs requires the knowledge of the noise autocorrelation. Moreover, in ATLAS conditions, to coincide the third sampling with the pulse maximum amplitude position we need to know the precise position in time of the physics signal for each cell. We will examine in the following these two aspects.

4 Study of the Arrival Time of the Signal (T0)

4.1 T0 definition

The T0 is defined as the time when a signal starts. For the calibration it depends only on the cable lenghts that bring the signal from the calibration board (where the signal is generated) to each cell, and from there to the FEBs (where the signal is amplified, shaped, sampled, pipelinized and digitalized), and on the different time delays found on the electronic boards found on the way. Once the T0 value is understood on the calibration signals, we'll be able to predict the arrival time of the signal of an incident particle (physics time), substracting the contribution from the calibration cable lenghts and taking into account the particle's time of flight depending on the cell's position.

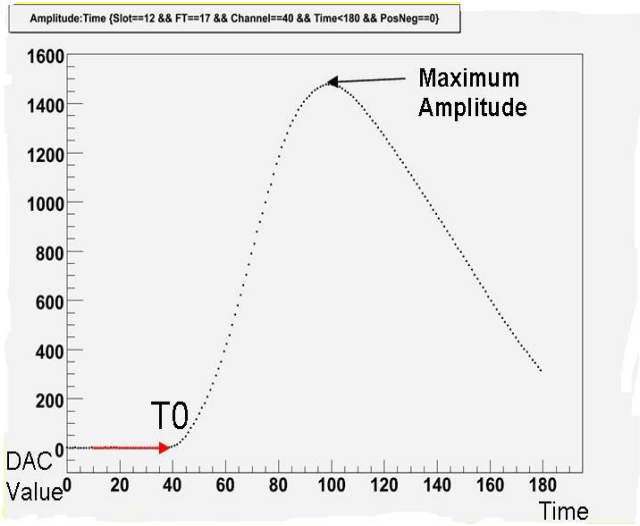

Figure 15: A calibration signal pulse showing its TO and its maximum amplitude.

To calculate the T0 we use the data of 'delay runs' corresponding to the injection of a known current. The obtained signal is pedestal substracted output of the FEBs in ADC counts. Each FEB gives the data of 128 cells, meaning 128 signals. The signals go from inside the cryostat to the FEBs via special tubes called Feed Through (FT). There are two FTs per module of the calorimeter (32 per semi-barrel), and each one 'feeds' 14 FEBs: 1 from the Pre-Sampler, 7 from the Front, 4 from the Middle and 2 from the Back.

We used as T0 the time at 0.2% of the maximum amplitude. This is a compromise between not to be influenced by the noise before the signal going lower and not to be sensitive to the signal shape depending on the cell capacitance going higher. Several definitions were made: 10%, 5%, 2% and 0.2%. After different tests we took the T0 calculation made taking the 0.2% on the time of the maximum amplitude of the signal for each cell (or channel), for it was the closest to the T0 expected from cable lenght computing (see below). This is made for all available data of the calibration runs.

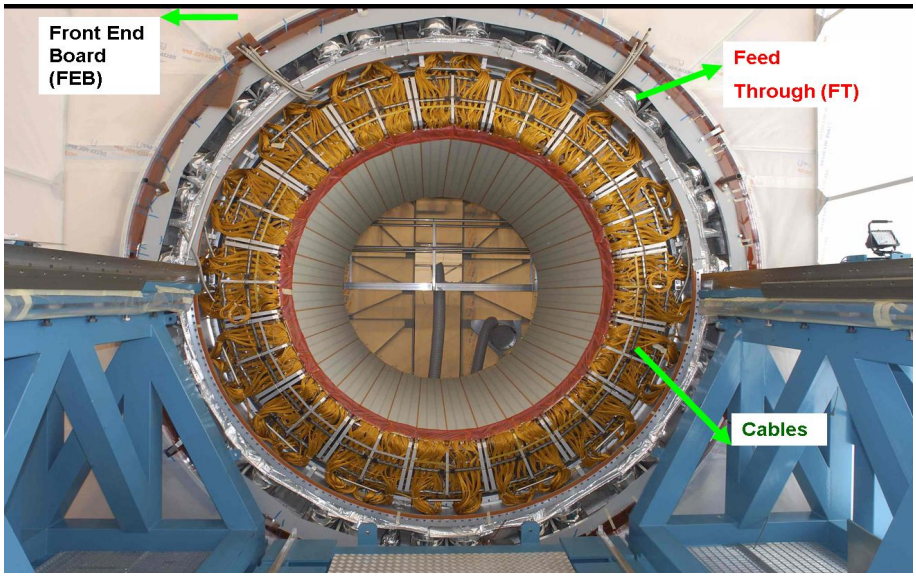

Figure 16: The barrel in its cryostat with the location of a FEB, FT and cables.

T0 expected The T0 expected is calculated knowing the cable lenghts that bring the signal from the calibration board to the FEBs and the signal speed in them. All the cables were measured and their value kept in a data base. The cables that distribute the calibration signal and the signal cables for the front section are all of 50 Ohms, with a signal velocity (cold measured) of 5.5 ns/m. All the other cables (signal cables for the middle and back sections) are of 25 Ohms, with a signal velocity of 6 ns/m.

Contribution from the Calibration Boards An expected time delay contribution comes from the calibration boards. Some internal delays give a dispersion of $\pm 1ns$ per channel. There is one board per FT, which means one value per channel per FT.

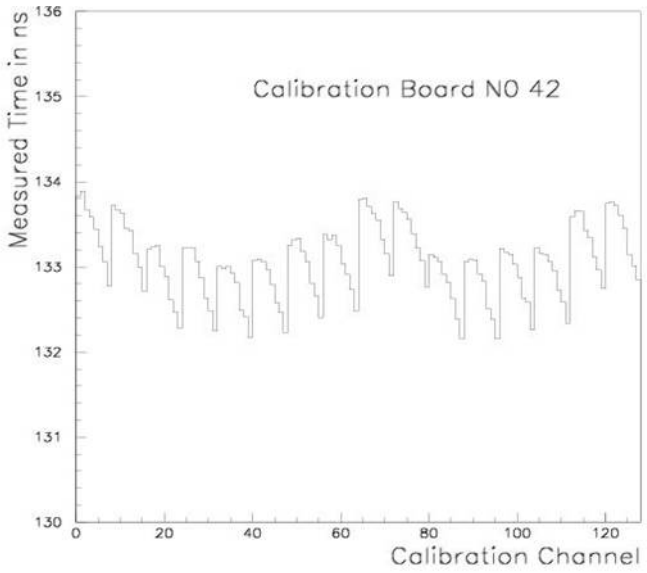

Figure 17: Intern delays on a calibration board showing the dispersions per channel.

4.2 Delays per FEB

When calculating and plotting the T0 values for several FTs, a dispersion of about 2 ns between them is found for each bunch of 128 channels (each FEB). There are and will be only 1600 channels studied, meaning 12 FEBs (7 from the front, 3 middle and 2 back) and 64 channels of a middle FEB per FT (the pre-sampler is not taken into account).
The plot has a systematic decreasing T0 shape that is due to the difference of cable lenghts for each section and their position in the electrode. For instance, the first 7 FEBs (channels 0 to 895) are from the front section, the following 2 (channels 896 to 1152) are the back section and the last 3 and a half (channels 1153 to 1600) are from the middle section. Non connected channels can be identified as those having zero value (a big vertical line).

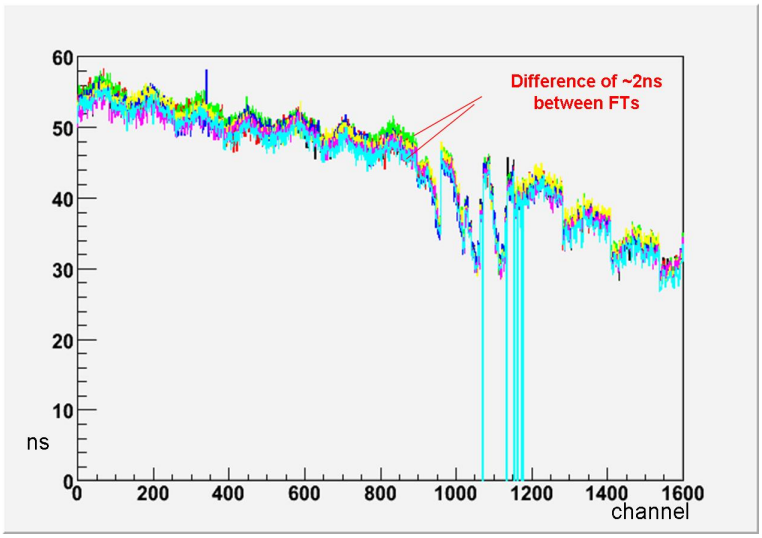

Figure 18: T0 for several FTs (one for each color) of barrel C. Vertical lines correspond to non connected channels.

Data coming from the FEB internal delays were already measured, and plotting its distribution we were able to find a dispersion of 1 ns from one FEB to the other. There is one entry per FEB (the 832 FEBs of the whole calorimeter, without the pre-samplers), but the mean value of the distribution depends on the test bunch. Some of the data was lost, that's why 36 FEBs have a null value.

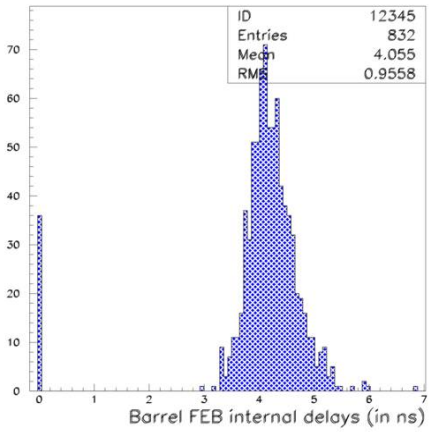

Figure 19: Ditribution of internal FEB delays, one value per FEB for the calorimeter.

To see if this internal delay was really a cause of the difference per FEB found before, we make a two dimentional plot containing, on the vertical axis, the difference value of the FEB internal delays with one of them as reference, and on the horizontal axis we take a FT as reference and make the FEB to FEB difference of that with the remaining FTs. This gives a quite large but useful anti-correlation, wich makes us certain that a cause of the time difference between the FEBs is due

to this internal delay studied.

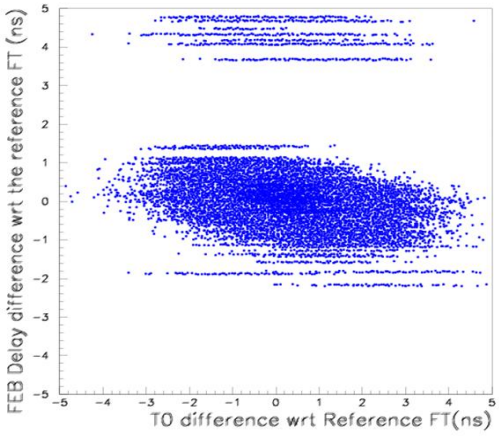

Figure 20: Correlation of internal FEB delays and FT time differences, using one FEB as reference.

We can see the T0 distribution for several FTs before and after adding the FEB delay correction. A little improvement was made, and can be clearly seen between the channels 600 and 800 (Front section).

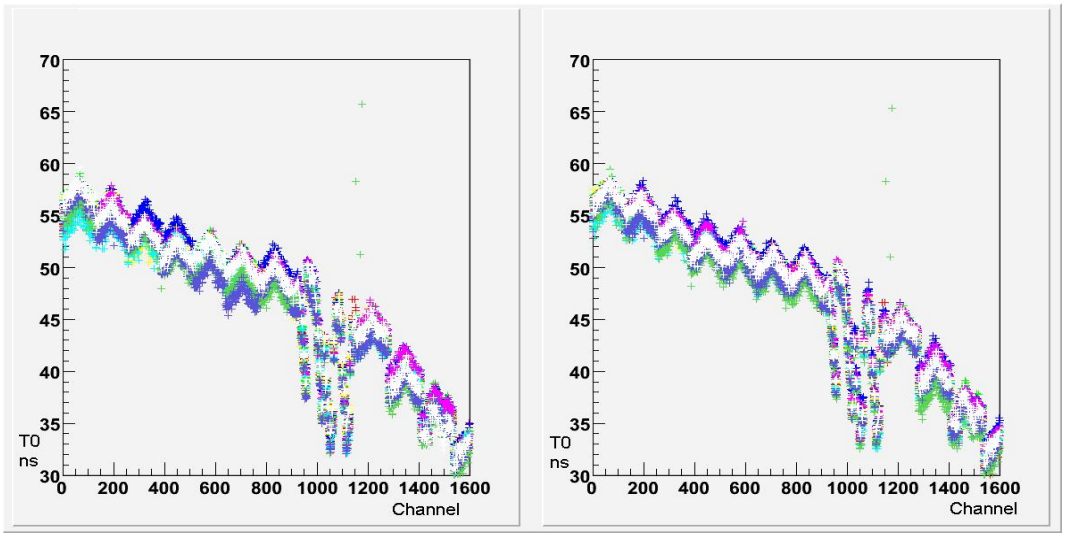

Figure 21: T0 calculated before (left) and after (right) internal FEB delay correction.

4.3 Systematic V shape

We show in figure 22 the average T0 after corrections for several FTs and we compare with the expected T0 given from cable lenghts. We first observe that the agreement between observation

and expectation is good within 1ns in the Front FEBs and within 2-4 ns in the back and middle. The second observation concerns a systematic shape like inverse V. This V shape must be understood, to know if it comes from the calibration path and will only be seen on the calibration, or if it actually comes from the FEB boards themselves and will be seen at the physics data.

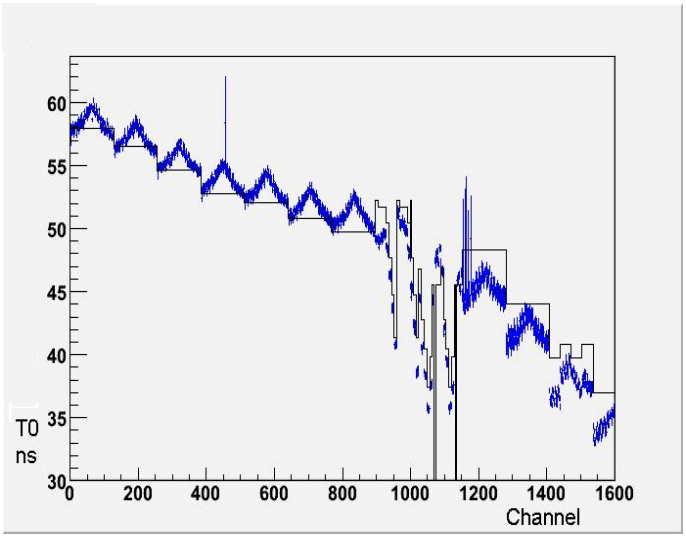

Figure 22: Expected T0 from cable lengths (black) and T0 found after all previous corrections (blue).

To confirm the origin of the V shape present on all the FEBs, we made a serie of experiments on the banc test found at LAL. This banc test was used to validate all the FEBs found on the calorimeter. We used the simplest setup on a test FEB there. To avoid any contribution from other electronics than the FEB itself, we inyected directly a known stable signal to the FEB input channel by channel. We did this by conecting a single cable from the signal generator, passing trough an attenuator to reduce the signal's amplitude to a measurable level, then connecting it to a channel on the FEB and perform a timing test with a software designed for that purpose. We repeated it for all the 128 channels and then measured: the time where the maximum amplitude is found (Tmax), and the T0 after pedestal substraction.

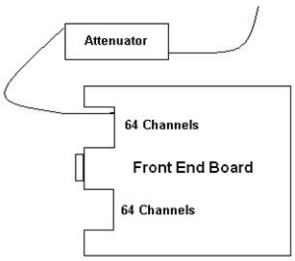

Figure 23: Setup of the experiment at LAL banc test.

The Tmax and T0 show a similar inverse V shape, and some structures having 2 ns peak to peak. This actually confirms the origin of the shape on the electronics of the FEB boards and will be seen on the actual physics data.

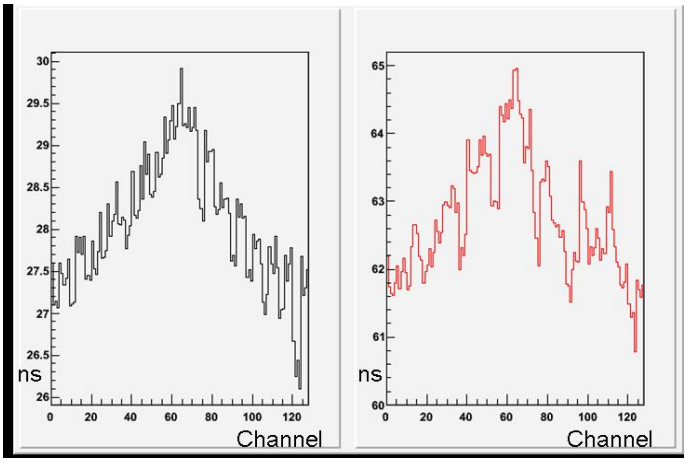

Figure 24: T0 (left) and Tmax (right) found with the LAL FEB data.

As a conclusion, cable lenghts fairly describe T0 distribution within 1-2ns for the front FEBs, and 3-5ns for Back and Middle ones. Additional investigations are needed to further understand the remaining differences.

5 Noise Autocorrelation Function Stability

As seen in Chapter 2, the autocorrelation must be know because it's required for the the OFC calculation, and though for the energy reconstruction. Take it into account leads to minimize the electronic noise in the energy calculation.

5.1 Autocorrelation Calculation

It turns out that the noise has a structure in time: the noise of a sample is correlated to the one of the next sample, the correlation being made by the covariance between both noises. The covariance matrix is then given by:

$$[Cov] = \begin{pmatrix} \sigma_1^2 & Cov_{12} & Cov_{13} & Cov_{14} & \dots \\ Cov_{21} & \sigma_2^2 & Cov_{23} & Cov_{24} & \dots \\ Cov_{31} & Cov_{32} & \sigma_3^2 & Cov_{34} & \dots \\ Cov_{41} & Cov_{42} & Cov_{43} & \sigma_4^2 & \dots \\ \vdots & \vdots & \vdots & \vdots & \ddots \end{pmatrix}$$

with

$$\begin{aligned} Cov_{ij} = & \sum_{i,j}^{N} \frac{(Noise_i - < Noise_i >)(Noise_j - < Noise_j >)}{N} \\ = & \sigma_i \sigma_j AC_{ij} \end{aligned} \tag{16}$$

where AC_{ij} is the correlation coefficient between the i and j samples. The noise level does not rely on time, so $\sigma_i = \sigma_j = \sigma \forall i \forall j$ and AC_{ij} only depends on $j - i$, the matrix can be simplified to give a symetric shape:

$$[Cov] = \sigma^2 \begin{pmatrix} 1 & AC_1 & AC_2 & AC_3 & \dots \\ & 1 & AC_1 & AC_2 & \dots \\ & sym. & 1 & AC_1 & \dots \\ & & & 1 & \dots \\ \vdots & \vdots & \vdots & \vdots & \ddots \end{pmatrix} = \sigma^2 \times [AC]$$

where AC_n is redefined as the correlation coefficient between the samples n and $n + i$. AC is the autocorrelation matrix.

Autocorrelation Data The Noise Autocorrelation Coefficients (NAC) are calculated using the noise of every sample and their covariance computed using eq.(16) after pedestal substraction. A sample is taken every 25 ns. We worked on noise autocorrelation values from 11 different pedestal runs: 8 at high gain (13239, 15398, 16354, 18657, 20733, 25209, 29142 and 32302), 2 at medium gain (15437 and 16366) and 1 at low gain (16375). Each file contained 6 calculated covariances per channel (cov(0,1..6)). The first value (cov(0,0)) was always normalized to 1, so it was not taken

into account. With this data we looked at: the autocorrelation shape, it's stability on time (per run number) and the effect of bad channels on it.

5.2 Autocorrelation shape

To study the autocorrelation shape we plotted the average value of each one of the six samples, the first value being of cov(0,1), for several FTs. This gives a shape that decreases on the second or third sample (cov(0,2) or cov(0,3)), where the minimum value is found, and then increases until getting kind of stable. The particular shape is given by the electronics of the calorimeter and the covariance calculation. Notice that for a given shaper, the covariance shape, and in particular the position of the minimum, depends mainly on the capacitance and the cable lenghts.

When we plot the same data but for only one FT we can see the dispertions given per channel. This is mainly due to the different cable lenghts, specially in the back section where the big dispertions can be seen.

The autocorrelation is also very sensitive to gain. We plotted three consecutive runs each one with different gain, we can see that NAC decrease from high to low gain. This can be explained due to the correlation NAC have with noise, and noise is differently amplified for every gain. On low gain the amplification is almost null, that's why the values are so small compared to the high gain that sees the preamplifier. All the following studies were done taking only high gain runs.

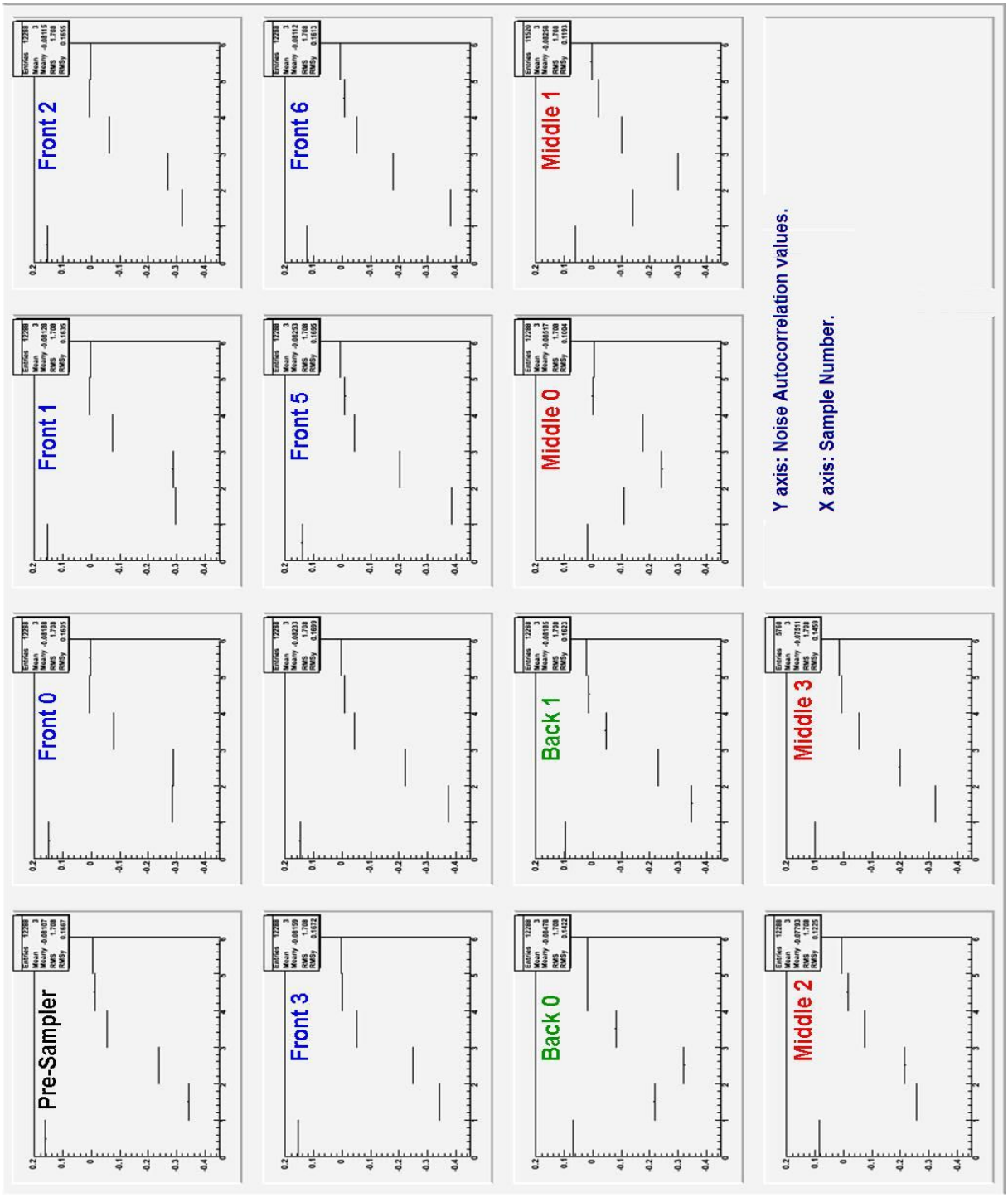

Figure 25: Mean value of autocorrelation per slot for 16 FT of barrel C (run 32302).

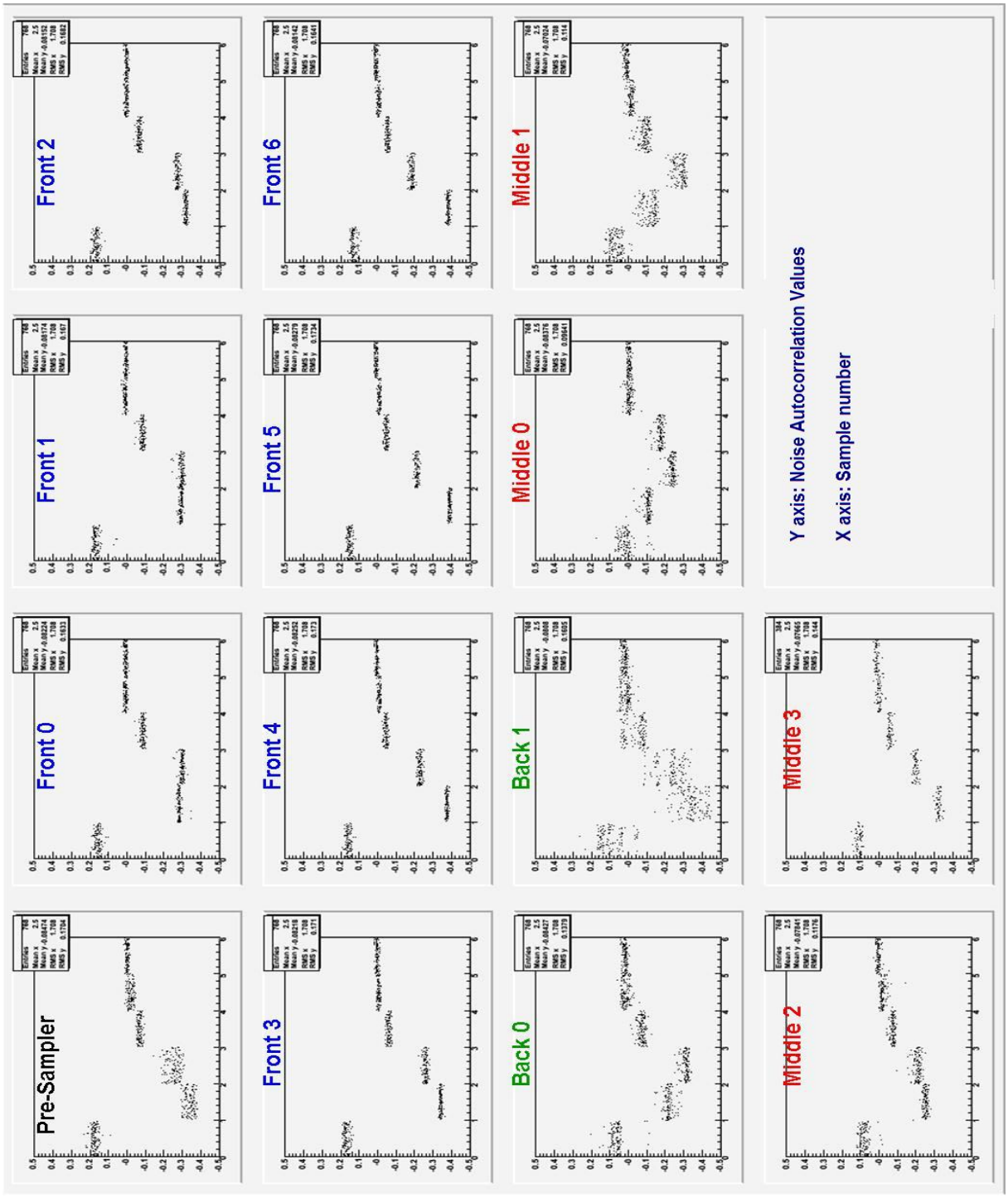

Figure 26: Noise Autocorrelation values per slot for FT5C showing the dispersions per channel.

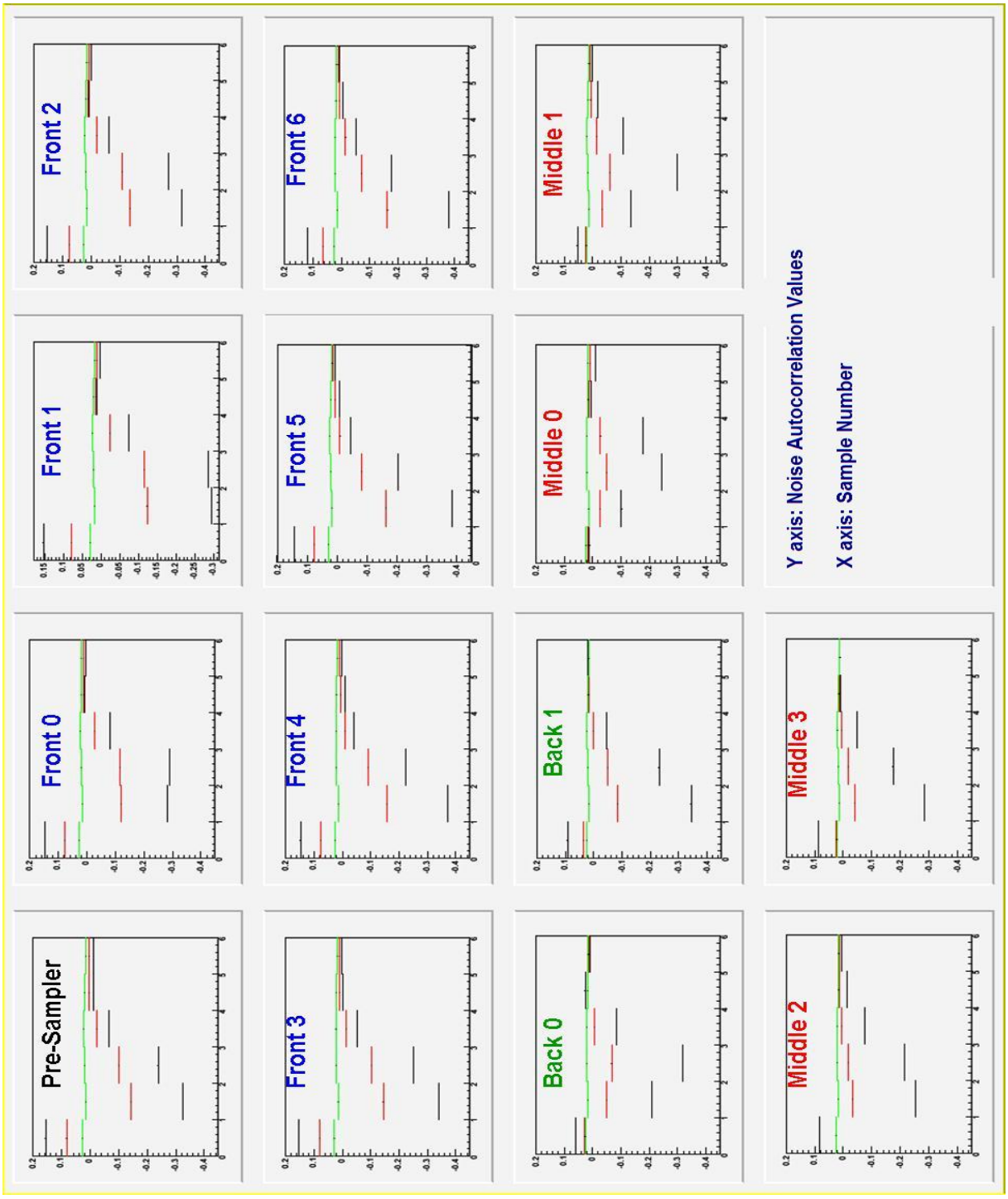

Figure 27: Mean autocorrelation value per slot for different FTs. In high (black), middle(red) or low (green) gain.

5.3 Autocorrelation Stability

To study the stability of the noise autocorrelation coefficients we took their channel by channel difference between two consecutive runs, for each sample, and plotted their distribution. The mean value was usually very close to zero, and the presence of some tails were observed.

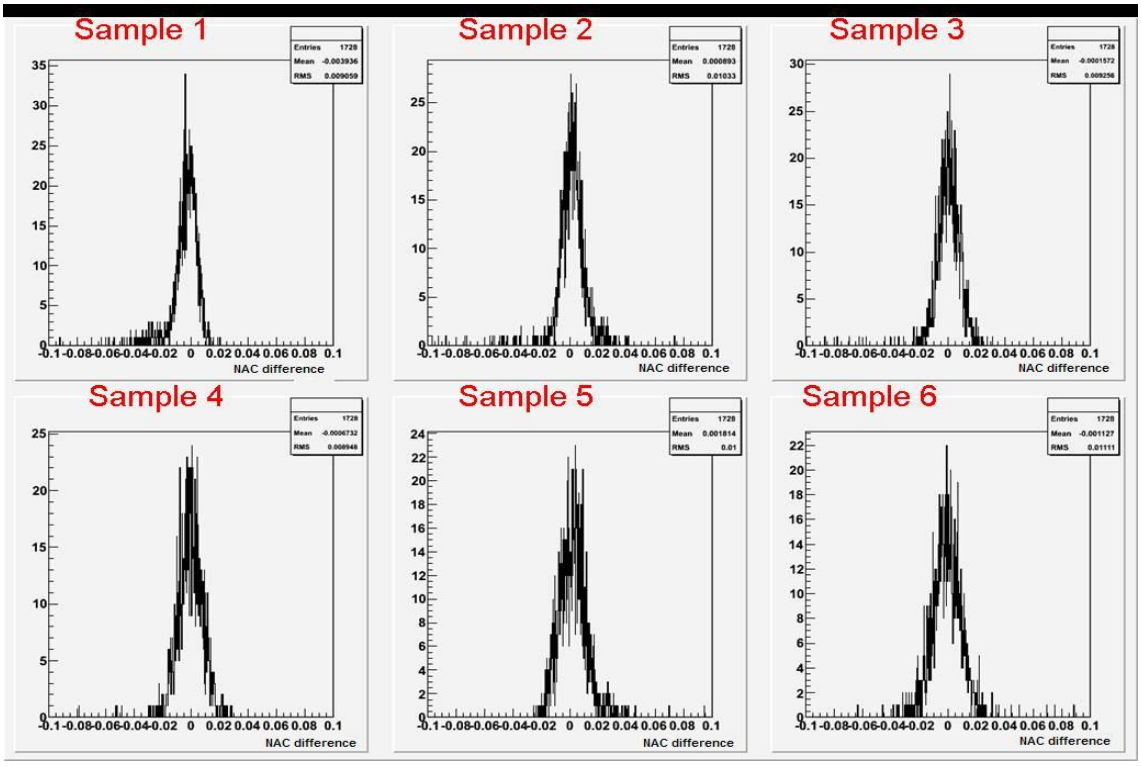

Figure 28: Distributions of channel by channel difference, per sample, of the NAC values between runs 29142 and 32302, on FT 18C.

Focusing on the first sample we plotted the same channel by channel difference for each FT between two consecutive runs. Then we fit the distribution by a gaussian to take away the tails contribution, and after this be able to take the mean value to study the stability of the first sample of NAC for all FTs.

We did this for all FTs with full history, meaning those with non-null value of autocorrelation in any of the runs. Plotting this mean value we obtain a distribution that contains 38 FTs on 7 consecutive runs. We can notice a mean stability value of 0.5%, taking the mean value for the first sample as 0.1, and extreme values (peak to peak) of $\pm 5\%$. There was a big variation between the run difference 25209-29142 that is responsable for most of the left tail on the distribution. This was due to the end of a special campaign for noise filters installation which improved indeed pick-up of noise by different cables.

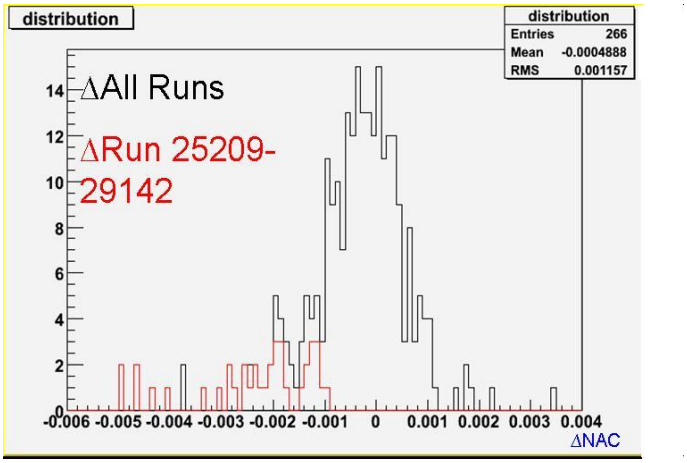

Figure 29: Mean Gaussian value distribution for 38 FT with full history along 7 runs.

Identifing some of the extreme values on the distribution, we decided to make another plot where they could be seen in a different way, so we plotted the NAC values per run difference for different FTs. One of them, FT18C, showed a big variation ($\pm 4\%$ peak to peak).

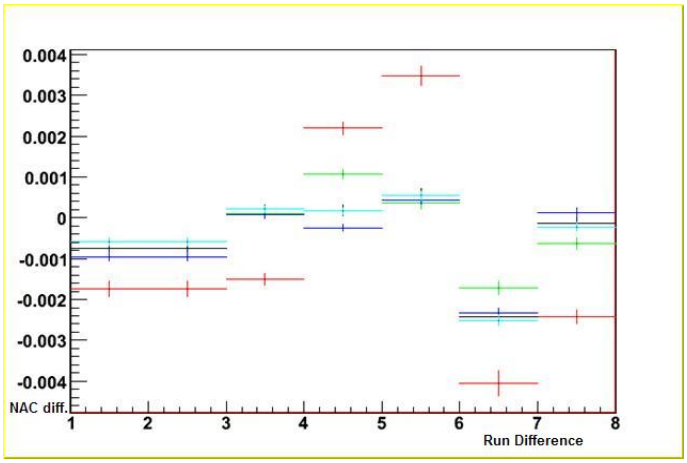

Figure 30: Autocorrelation Value per run difference for several FTs (one of each color). FT18C is represented in red.

Run differences from left to right: 13239-15398, 15398-16354, 16354-18657, 18657-20733, 20733-25209, 25209-29142, 29142-32302.

FT18C problem On the difference between runs 25209 and 29142 for the FT18C a big tail appeared, that when taking the run difference 29142-32302 dissapeared.

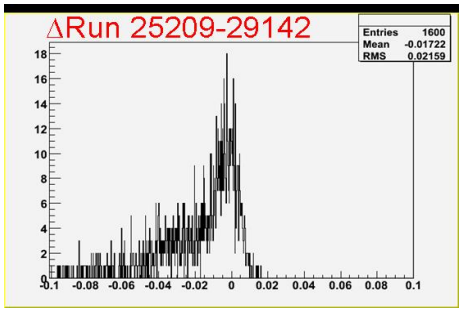

Figure 31: NAC difference on FT 18C for runs 25209-29142.

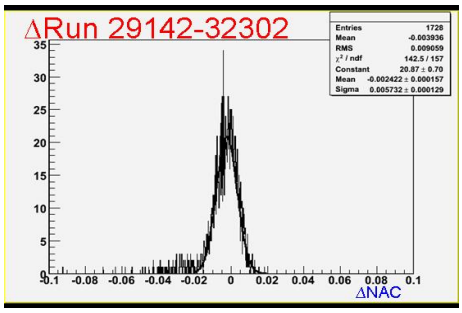

Figure 32: NAC difference on FT 18C for runs 29142-32302.

Looking at the noise and autocorrelation for the first two runs a big difference was seen: there was a higher noise on the first 64 channels that greatly affected the autocorrelation values. This showed the big correlation between the two, and how we could identify problems looking at the NAC.

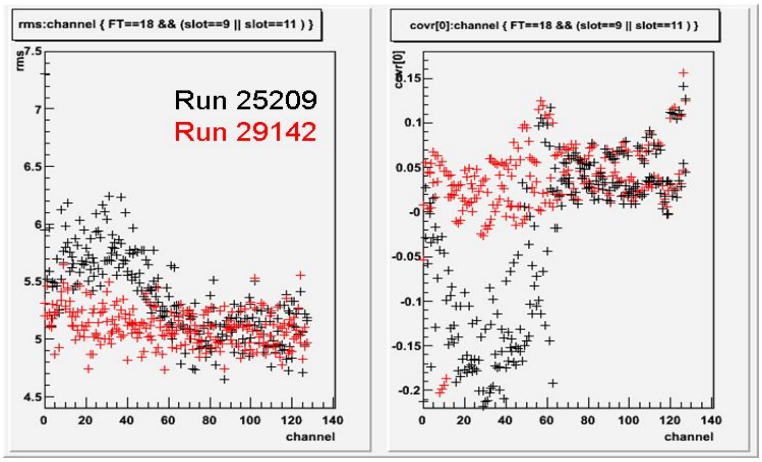

Figure 33: Noise (left) and Autocorrelation (right) values per channel of a middle slot, for runs 25209 (black) and 29142 (red).

This problem appeared in all runs previous to 29142 and was succesfully corrected.

5.4 Bad channels identification

Focusing on the first sample we also tried to identify some of the channels found on the distribution tails.

Some of the channels found on tails corresponded to ”faulty shapers”. Indeed, some shapers (of the order of 2% of the total number) have been observed to change their characteristic time. The observation was a change of the amplitude and shape of the corresponding calibration pulse. The autocorrelation values were plotted for two consecutive runs where some were identified with faulty shapers, and the X% of the difference between samples calculated to correlate it with the difference of amplitude between both runs.

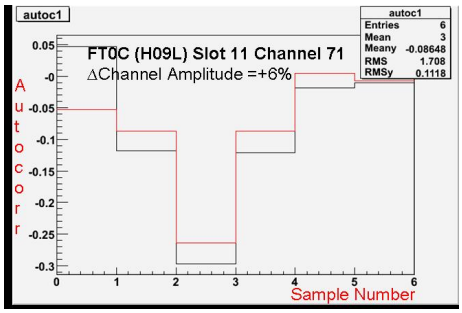

Figure 34: NAC value per sample number for two runs: 18657 (black) and 25209 (red) on one of the many channels found.

Taking only the NAC difference values of the first sample (runs 18657 and 25209) that were found on tails, we plotted them with those having an amplitude difference value $> 2\%$. A correlation was found: the NAC difference values increase when the amplitude increases.

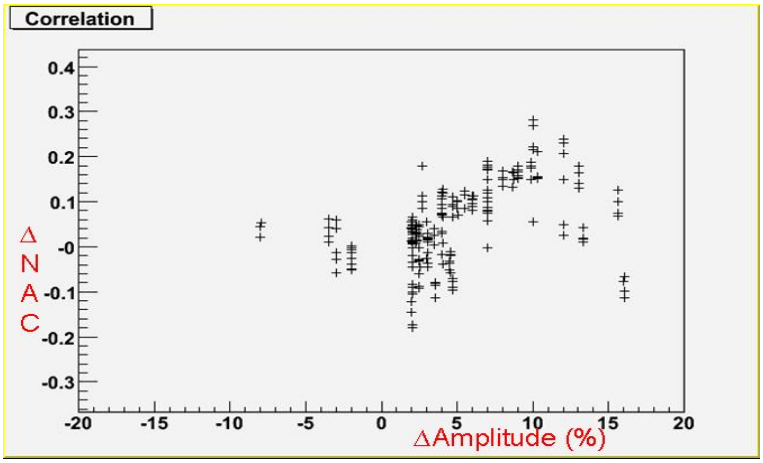

Figure 35: Correlation between the NAC difference and the Amplitude's change %.

Looking at the pulse shapes we found that: when the amplitude>0 and the NAC difference was >0, then the amplitude decreased for the second run, and when the amplitude>0 and the NAC difference was <0 then the amplitude also decreased for the second run but the pulse shape was also distorded.

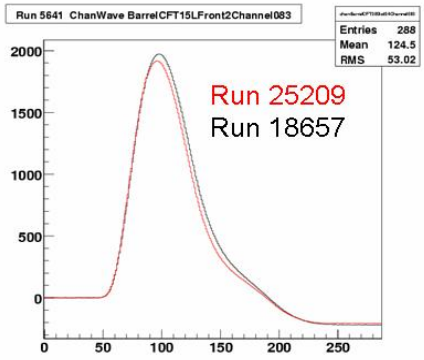

Figure 36: The signal pulse from the same channel for two different runs showing the amplitude's change.

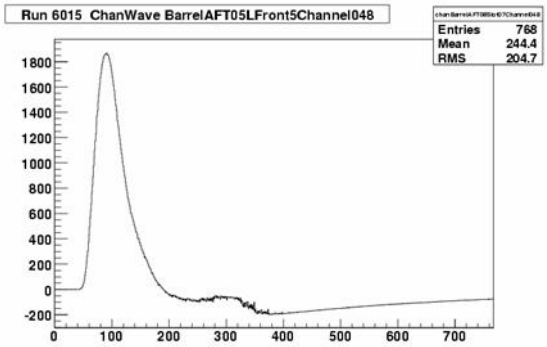

Figure 37: A distorted pulse given when $\Delta NAC < 0$ and $\Delta Amplitude > 0$.

A very interesting thing was found when only looking at the autocorrelation values per channel. Even when plotting these values per channel we were able to identify very easily the bad channels and the faulty shapers, just looking at those found outside the bulk. This is specially true for the first and second autocorrelation sample where it's more clearly seen.

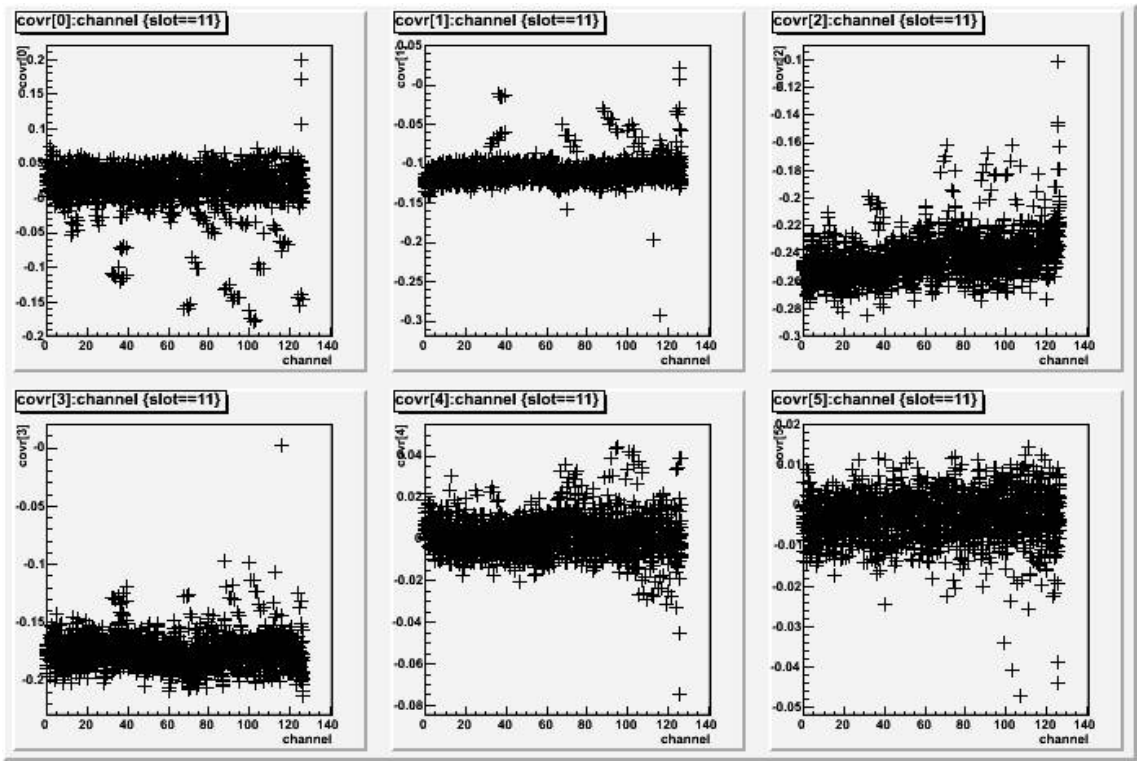

Figure 38: Typical autocorrelation per sample values for all channels of M0.

FT5A problem Looking at the channels on the distribution tails we were able to identify another FT with noise problems between runs 29142 and 32302. The FT5A showed a superior noise for

channels > 70 on the run 32302, that could be clearly seen on the autocorrelation values.

Figure 39: Noise and Autocorrelation values per channel for the middle slots, for runs 29142 and 32302

When making the noise and autocorrelation difference between both runs the problem was seen more clearly, specially on the autocorrelation one. It seems that the autocorrelation is a lot more accurate to identify the problems than the noise itself. Both noise and autocorrelation, as expected, showed a strong correlaton.

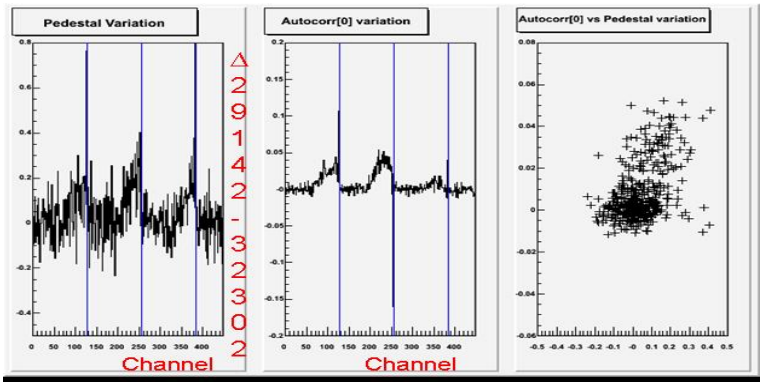

Figure 40: Noise (left) and autocorrelation differene per channel. The correlation between the two is shown on the right.

Given the increasing number of faulty shaper appearance, the collaboration decided to take out all FEBs and cure the whole number of shapers by freezing their characteristic time. This major operation concerned the whole calorimeter and took place during few months between end 2007 and March 2008.

6 Conclusions

The electromagnetic calorimeter calibration is necessary to obtain the good OFC needed for energy and event reconstruction of the incident particles. Our study was focused on two principal aspects needed to calculate the energy and time of a calorimeter's cell: its arrival time (T0), which allows the correct sampling of the maximum of the signal, and its autocorrelation noise coefficient, which is used in the OFC calculations.

The arrival time of the calibration signals (T0) is being well represented using the cable lenghts and the internal electronic boards delays, with a difference of 1 to 2 ns on the front sections and 3 to 4 ns on the middle and back sections. This will be certaintly improved after the first data takings, with a final goal of a few hundreds of pico-seconds.
The dispersion seen for a given channel on the T0 calculation, between FTs, comes partially from the corresponding FEBs. The inverse V shape was confirmed as coming from the internal FEB electronic structure and not from the calbration path, and so will be seen on the data taking of physics events. An electronics correction is not foreseen, but being aware of it's presence will allow an accurate timing measurement and so a good event and energy reconstruction.

The stability of the autocorrelation function is strongly linked to the noise stability and the absence of bad channels in the calorimeter. This will be followed up regularly on the data taking and the pedestal set records. The NAC seem to be very good detectors of bad channels and faulty shapers. This study will be repeated with the data taken after the shapers repair on the FEBs.

References

[1] Coughlan, G. and Dodd, J. and Gripaios, B. *The Ideas of Particle Physics. An Introduction for Scientists*, Third Edition, Cambridge University Press, 2006, 189-203.

[2] www.cern.ch

[3] The ATLAS Collab. *ATLAS Detector and Physics Performances, Technical Design Report I.* CERN/LHCC/99-14

[4] The ATLAS Collab. *ATLAS Detector and Physics Performances, Technical Design Report II.* CERN/LHCC/99-15

[5] The ATLAS Collab. *ATLAS Liquid Argon Calorimeter Technical Design Report.* CERN/LHCC/96-41

[6] Lechowski, M. *Test du Modèle du "Petit Higgs" dans ATLAS au LHC Simulation de la numérisation du calorimètre électromagnétique.* LAL/05-20.

[7] Prieur, D. *Etalonnage du calorimètre électromagnétique du détecteur ATLAS. Reconstruction des événements avec des photons non pointants dans le cadre d'un modèle supersymétrique GMSB.* LAPP/T-2005-03.

[8] Cleland, W.E. and Stern, E.G. *Signal processing considerations for liquid ionization calorimeters.*Nucl. Instrum. Meth. A338 (1994) 467-497.